




# JGR Solid Earth

## RESEARCH ARTICLE

10.1029/2021JB022573

# Semi-Brittle Deformation of Carrara Marble: Hardening and Twinning Induced Plasticity

E. Rybacki<sup>1</sup> , L. Niu<sup>1,2,3</sup> , and B. Evans<sup>4</sup> 

<sup>1</sup>GFZ German Research Centre for Geosciences, Potsdam, Germany, <sup>2</sup>Institute of Geology, China Earthquake Administration, Beijing, China, <sup>3</sup>Hebei Earthquake Agency, Shijiazhuang, China, <sup>4</sup>Massachusetts Institute of Technology, Cambridge, MA, USA

### Key Points:

- The mechanical behavior and microstructure evolution of marble was studied in triaxial compression tests over a wide range of conditions
- Semi-brittle deformation occurred by strain partitioning amongst cataclasis, twinning, and dislocation motion over all conditions
- At temperatures between  $\approx 200$  and  $400^\circ\text{C}$ , changes in strain rate and pressure had reduced influence on strength and hardening

### Supporting Information:

Supporting Information may be found in the online version of this article.

### Correspondence to:

E. Rybacki,  
[erik.rybacki@gfz-potsdam.de](mailto:erik.rybacki@gfz-potsdam.de)

### Citation:

Rybacki, E., Niu, L., & Evans, B. (2021). Semi-brittle deformation of carrara marble: Hardening and twinning induced plasticity. *Journal of Geophysical Research: Solid Earth*, 126, e2021JB022573. <https://doi.org/10.1029/2021JB022573>

Received 8 JUN 2021  
Accepted 23 NOV 2021

**Abstract** Semi-brittle flow occurs when crystal plasticity and cataclastic mechanisms operate concurrently and may be common at mid-levels of the Earth's crust. Using a Paterson gas-deformation apparatus, we performed 67 conventional triaxial deformation experiments on dry samples of Carrara marble in the temperature range of  $T = 20\text{--}800^\circ\text{C}$ ; confining pressures ( $P_c$ ) were 30, 50, 100, 200, and 300 MPa, and strain rates ( $\dot{\epsilon}$ ) were  $10^{-3}$ ,  $10^{-4}$ ,  $10^{-5}$ , and  $10^{-6}$  s<sup>-1</sup>. Axial strains ( $\epsilon$ ) were  $\lesssim 0.12$ . The measured (differential) stress,  $\Delta\sigma = \sigma_1 - P_c$ , changes with strain at most applied conditions. At  $\epsilon = 0.05$ , both stress and the hardening coefficient ( $h$ ), that is, the rate of increase of stress with strain, increase as  $T$  decreases and  $P_c$  increases. At  $T \lesssim 400^\circ\text{C}$ ,  $h$  is quite large and the sensitivity of  $\Delta\sigma$  on  $\dot{\epsilon}$  is low, while both are sensitive to increasing pressure. In this temperature range, the mechanical behavior of the marble is very similar to that exhibited by high-strength, high-ductility, hexagonal metals that deform by processes called twinning induced plasticity (TWIP). Twinning and dislocation motion are abundant in the samples, as are inter- and intracrystalline microfractures. The concurrent activation of these deformation mechanisms leads to complex relationships of  $\Delta\sigma$  and  $h$  with the applied  $T - P_c - \dot{\epsilon}$  conditions. This behavior suggests that peak stresses for calcite rocks deforming by semi-brittle processes will occur at  $P_c - T$  conditions of the middle crust, and that they might be more strongly influenced by total strain rather than by strain rate.

**Plain Language Summary** Natural deformation of rocks at shallow depth is expected to be dominated by (micro-) fracturing, whereas deeper within the Earth's crust, crystal-plastic mechanisms probably dominate. Semi-brittle flow, which involves the concurrent operation of both sets of deformation mechanisms, is probably common in the middle crust. To better understand this mechanical behavior, we deformed Carrara marble samples over a wide range of temperatures, pressures, and strain rates. The stress supported by the marble changes as inelastic strain increases and generally increases with increasing pressure and decreasing temperature at a given strain. Strain rate had a small influence on stress at temperatures  $\lesssim 400^\circ\text{C}$ . This mechanical behavior is quite comparable to that of some hexagonal metals, which deform by a process called twinning induced plasticity at temperatures below about half the melting point. The microstructure of the marble samples shows that three deformation mechanisms are operating: Twinning, dislocation motion, and microfracturing. The relative intensity of these mechanisms depends on deformation conditions. The correlations between applied conditions and mechanical response that we observed suggests that strength of calcite rocks in the middle crust is indeed governed by semi-brittle processes and depends more on total strain and less on variations of strain rate.

## 1. Introduction

The strength and associated deformation processes of the continental crust depend mainly on lithology, water content, (effective) confining pressure ( $P_c$ ), temperature ( $T$ ), and strain rate ( $\dot{\epsilon}$ ). All of these parameters might vary with depth. Commonly, a strength-depth profile is approximated by assuming brittle frictional sliding or failure in the upper part of the crust and crystal-plastic flow in the lower portion (e.g., Brace & Kohlstedt, 1980; Goetze & Evans, 1979; Kohlstedt et al., 1995; Regenauer-Lieb et al., 2006; Scholz, 1988; Shimada, 1993). Predicting strength in the middle portions of the continental lithosphere requires numerous assumptions associated with mineralogy, loading configuration, and the presence of fluids. Not surprisingly, estimates of the strength profiles vary widely. For an example, see discussion by Bürgmann and Dresen (2008). One major problem is the lack of a robust constitutive model at intermediate depths. Rock strength becomes more difficult to predict because, as depth increases, the dominant deformation mechanisms change from pressure-dependent, brittle processes

© 2021 The Authors.

This is an open access article under the terms of the [Creative Commons Attribution-NonCommercial License](https://creativecommons.org/licenses/by-nc/4.0/), which permits use, distribution and reproduction in any medium, provided the original work is properly cited and is not used for commercial purposes.

to crystal-plastic mechanisms that are relatively pressure-independent, but sensitive to temperature. The region where deformation mechanisms include both fracturing and crystal plasticity is often called the semi-brittle region (Carter & Kirby, 1978). When deformation is dominated by crystal plasticity, and local cataclastic processes are insignificant, the material is often said to have undergone the brittle-plastic transition.

When observed at larger scales, the deformation mode often appears to be “ductile”, meaning that deformation is not localized along a discrete fracture zone. In metal science, however, also discrete fracturing is said to be ductile, when crystal-plastic micromechanisms dominate, for example, by the growth of voids (e.g., Ashby et al., 1979). The relation between non-localized ductile deformation and semi-brittle flow where both micro-scale processes are occurring, is important, but not completely straight-forward. For example, localization may be absent when deformation involves only microfracturing (e.g., Tullis & Yund, 1992). Conversely, localized deformation may involve only crystal-plastic processes operating in a small spatial zone. Note that from the engineering point of view, the “brittleness” of rocks is often described by various index definitions that may be based on composition, elastic properties, or deformation characteristics, but that term does not indicate the prevailing deformation mechanisms (e.g., Hucka & Das, 1974; Rybacki et al., 2016). Even the terminology used to describe such deformation is problematic. Here, we follow the definitions given by Rutter (1986): The term “semi-brittle” is used to imply that both crystal-plastic and local-scale, cataclastic processes are operating; “ductile deformation” identifies non-localized deformation, regardless of which mechanisms operate. The term “brittle-ductile transition” is used for the transition between failure occurring within a localized region and failure occurring over a broad region, without reference to mechanisms. For various aspects of this discussion, see Evans et al. (1990); Heard (1960), Meyer et al. (2019), Rutter (1986), and Tullis and Yund (1992).

Semi-brittle flow is expected to be a common deformation mode in mid- to upper- levels of the crust, and field evidence of its occurrence in the Earth's crust is manifold (e.g., Babai & La Tour, 1994; Dresen et al., 1997; Gapais, 1989; Ross & Lewis, 1989; Stewart et al., 2000; Takagi et al., 2000). This deformation mode may occur over a wide range of temperatures and pressures, particularly in polyphase rocks, when the weak phase is deforming by crystal-plastic mechanisms, but the stronger constituents are still brittle (Evans et al., 1990). Numerous laboratory experiments in the semi-brittle regime have been performed on multi-phase rocks and aggregates (e.g., Bos & Spiers, 2002; DellAngelo & Tullis, 1996; Herrmann et al., 2018; Odedra et al., 2001; Pec et al., 2016; Ross & Wilks, 1995; Rybacki et al., 2017; Rybacki et al., 2015; Siddiqi et al., 1997; Tullis & Yund, 1992; Violay et al., 2012; Wendt et al., 1998). Semi-brittle deformation can also occur in single-phase rocks (Brantut et al., 2011; Chester, 1988; Kirby & Kronenberg, 1984; McLaren & Pryer, 2001; Richter et al., 2018; Schmocker et al., 2003).

Some attempts have been made to predict the strength of polymineralic rocks in the semi-brittle regime using empirical mixing relations (e.g., Handy et al., 1999; Noda & Shimamoto, 2010). However, owing to the complex interplay between the different deformation mechanisms, developing a robust constitutive equation for semi-brittle deformation, even for single phase rocks, appears to be difficult. Several notable efforts have been made to develop a more inclusive constitutive law appropriate for temperatures intermediate between brittle behavior and crystal-plastic flow. In the temperature range of 120–400°C and 200 MPa confining pressure, Covey-Crump (1994, 2001) described the inelastic deformation of Carrara marble in terms of Hart's mechanical equation of state, assuming that all deformation occurred via low-temperature crystal plasticity. More recently, Nicolas et al. (2017) considered linear combinations of processes involving brittle crack propagation and dislocation slip during low temperature deformation of limestone. They successfully applied their model to results from room temperature experiments of brittle and semi-brittle creep of Tavel limestone.

The transition of the dominance from brittle to plastic mechanisms in single-phase rocks can be easily studied in calcite marbles because the pressure-temperature conditions necessary for the transition are relatively accessible in the laboratory. Because marbles are often structurally important, and because rocks of uniform grain size and simple mineralogy are easily available, numerous high temperature ( $T \geq 600^\circ\text{C}$ ) triaxial deformation and torsion studies have been performed on Carrara marble and Solnhofen limestone (e.g., Barnhoorn et al., 2004; Bruijn et al., 2011; Covey-Crump et al., 2016; de Bresser et al., 2005; Ferguson, 1983; Quintanilla-Terminel & Evans, 2016; Rutter, 1995; Rutter & Schmid, 1975; Rybacki et al., 2014; Schmid et al., 1977; Schmid et al., 1980; ter Heege et al., 2002; Valcke et al., 2015; Xu & Evans, 2010). Most of these have focused on obtaining steady-state creep laws for crystal-plastic deformation. Typically, these constitutive equations relate strain rate to (differential)

stress and other state variables (c.f., Equations 1 and 2 in Section 3.1.2). In addition, the experiments are often used to examine the role of external and internal boundary conditions on the evolution of microstructure.

At temperatures higher than 600°C, quasi-steady-state flow stress is usually obtained after a few percent deformation in triaxial compression test. But, modest hardening can continue up to shear strains of about 1.0. Straining above this value is accompanied by recrystallization and moderate strain weakening until a constant strength is achieved after a shear strain of about 4–5 (Barnhoorn et al., 2004; Pieri, Burlini, et al., 2001; Pieri, Kunze, et al., 2001). It is interesting to notice that fitting a power law to the triaxial deformation data for Carrara marble often yields high stress exponents ( $\geq 5$ ), which are incompatible with creep controlled by dislocation climb (Paterson & Olgaard, 2000; Pieri, Burlini, et al., 2001; Schmid et al., 1980). In addition, strength is slightly pressure dependent when  $T = 800^\circ\text{C}$  at a constant strain rate of  $10^{-5} \text{ s}^{-1}$  (de Bresser, 2002). This pressure sensitivity persists up to  $T = 900^\circ\text{C}$  when  $P_c < 50 \text{ MPa}$  (Nardini et al., 2020).

At lower temperatures, previous examinations in the semi-brittle regime have focused on examining dilatancy and micromechanics as a function of pressure over a range of temperatures. At room temperature, dilatant brittle processes, as indicated by pressure-dependent strength, the presence of microcracks in microstructural studies, or direct measurements of volumetric strain have been observed in Carrara marble up to about 400 MPa confining pressure when the rocks are deformed at room temperature (Edmond & Paterson, 1972). Direct measurements of volumetric strain indicate that dilatancy is present at temperatures up to 600°C (Fischer & Paterson, 1989). At low confinements and room  $T$ , strong dilatancy preceding localized failure is typically linked to a low (or even negative) hardening coefficient ( $h$ ), that is, the slope of the stress-strain curve, at a given  $\epsilon$  or  $\Delta\sigma$ . For example, at room temperature, both Solnhofen limestone and Carrara marble show strain weakening and/or failure when  $P_c$  is less than 100 MPa. As  $P_c$  is increased above this value, the rocks show positive hardening coefficients (Fredrich et al., 1989; Heard, 1960; Rybacki, 1986). When Carrara marble is deformed at room temperature and  $P_c = 30\text{--}450 \text{ MPa}$ , the dominant deformation processes in this regime are microcracking, twinning and dislocation glide (Fredrich et al., 1989). In addition to pressure-dependence of strength, brittle damage can be identified by a reduction of ultrasonic velocity measured during inelastic deformation (Schubnel et al., 2006; Schubnel et al., 2005).

Here, we present mechanical data and preliminary microstructural observations for Carrara marble, deformed at pressures of 30–300 MPa, temperatures from 20–800°C, and strain rates of  $10^{-3}$  to  $10^{-6} \text{ s}^{-1}$ . This  $P_c$ – $T$  range covers the full span of brittle to plastic transformation, helping us to constrain the influence of boundary conditions on the mechanical behavior and on the partitioning of deformation mechanisms. It is useful to be able to compare results of tests for samples of a single rock type that use a consistent technique on a single mechanical apparatus. At fixed  $P_c$ – $T$ – $\dot{\epsilon}$  conditions, strength, that is, the (differential) stress sustained by the rock at given strain, is transient and evolves with strain. We characterize the measured stress-strain curves by specifying the stress and hardening coefficient at  $\epsilon = 0.05$ , denoted by  $\Delta\sigma_{0.05}$  and  $h_{0.05}$ , respectively. All three parameters,  $P_c$ – $T$ – $\dot{\epsilon}$ , influence the mechanical behavior over the entire range of conditions. However, both strength and hardening coefficient have highly varying sensitivities to the three environmental parameters. We contend that semi-brittle deformation in calcite rocks depends on the interplay of all three deformation mechanisms, cracking, dislocation flow, and twinning. We intend to supplement this study with a new set of detailed microstructural analyses and to use these works to produce an improved micromechanical model.

## 2. Experimental Methods

Conventional triaxial compression experiments were performed on samples of Carrara marble (Bianco Loro, Apuane Alps, Italy), a standard material often used for laboratory deformation tests on calcite rocks. The starting material is almost undeformed, showing only minor undulose extinction, slightly sutured grain boundaries, low twin and dislocation density, and nearly random crystallographic preferred orientation (CPO) (Rybacki et al., 2013). The marble is composed of >99% calcite grains with an average grain size of about 220  $\mu\text{m}$  with low porosity (<0.8%) (c.f., Figure S1 in the Supporting Information S1). For deformation experiments, cylindrical samples of 20 mm length and 10 mm diameter with parallel end faces oriented perpendicular to the cylinder axis were prepared by grinding with fine-grit diamond wheels.

After preparation, all samples were stored in an oven at 50°C. Prior to testing, they were sealed against argon confining pressure using copper jackets about 0.3 mm thick. For the experiments, we used a Paterson gas deformation

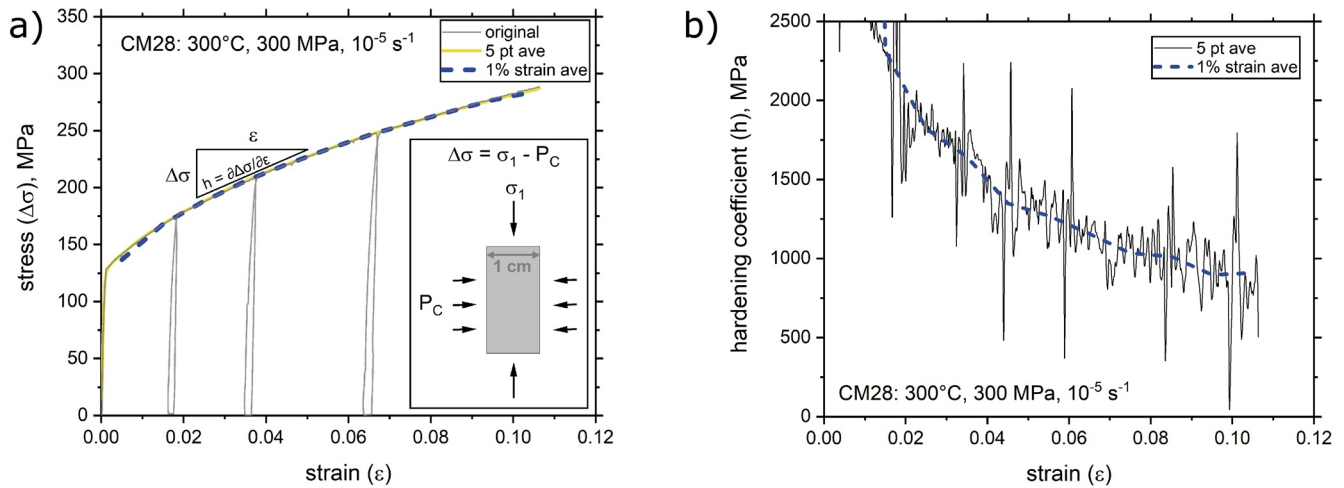


**Figure 1.** Typical stress-strain (a) and hardening coefficient-strain (b) curves. The sample was repeatedly unloaded to evaluate the unloading and reloading modulus after certain strain intervals. Original stress-strain data (thin gray line) were smoothed using a 5-point moving average (thick yellow line) as well as by a moving average over a strain interval of 0.01 (thick blue broken line). This averaging greatly reduces the noise of the calculated values for  $h$ . The inset in (a) shows schematically the notation of stresses applied to the cylindrical sample of 1 cm diameter and 2 cm length. Deformation conditions ( $T$ ,  $P_C$ ,  $\dot{\epsilon}$ ) are indicated.

apparatus, provided with an internal load cell (Paterson, 1970). The measured axial force was corrected for the load supported by the copper sleeve, which was determined using calibration runs on solid copper samples under similar conditions as for the deformation tests. Axial (differential) stress,  $\Delta\sigma = \sigma_1 - \sigma_3$ , was calculated from the corrected axial force and confining pressure ( $P_C = \sigma_3$ ), assuming homogeneous, constant-volume deformation (see inset in Figure 1a). Due to uncertainties related to load cell precision, jacket correction, and sample bulging, estimated accuracy of reported stress is better than 4% for individual runs. The axial strain,  $\epsilon$ , was derived from the measured axial displacement using a linear variable displacement transducer (LVDT, Schaevitz DC-E), corrected for (pressure and temperature-dependent) apparatus distortion, and subsequently converted to natural strain ( $\epsilon = -\ln(1-e)$ , where  $e$  is engineering strain). Sampling rate was 1 kHz. Initial settling of the relatively long and compliant piston assembly resulted in variations of the modulus measured below yielding. This effect was partially corrected by adjusting the stress-strain curves obtained at similar temperature to a common strain value just below the yield point. Due to this procedure, the accuracy of the absolute strain is  $\lesssim 0.001$ . Temperature readings, measured using a thermocouple located 3 mm above the top of samples, are accurate to within 1%. The temperature gradient along the sample was less than 2–3°C.

For most experiments done at temperatures between 200 and 600°C, samples were repeatedly unloaded and reloaded to estimate the evolution of Young's modulus with increasing deformation (Figure 1a). Upon reloading, the axial stress was re-established within short strain intervals that increased with increasing temperature, perhaps due to rapid healing of lattice defects during unloading at high  $T$ . However, owing to uncertainties caused by the low apparatus stiffness and the hardening of the (Cu) jacket with strain, we have not examined this data in detail. Therefore, for better legibility, these unloading-loading cycles are largely removed from shown stress strain curves. All corrected and cleared stress-strain data were smoothed using a rolling average algorithm; the number of points in the average varied, but in all cases, the strain interval of the average was  $\leq 0.001$ . From the local slope of such smoothed curves, we obtained the hardening coefficient,  $h = \partial\Delta\sigma/\partial\epsilon$  (Figure 1). Since curves of  $h$  vs. strain were relatively noisy, we further smoothed  $h$  values over a rolling interval of 0.01 in natural strain. This treatment greatly reduces the noise. At high strain ( $\approx 0.1$ ) the uncertainty of smoothed  $h$  was usually below about 5%, but it may be up to 25% in some exceptional circumstances (Figure 1b).

The samples deformed in the Paterson apparatus are denoted as CMxx, where xx is a numerical identifier. Each sample was deformed up to strains of about 0.12 at constant displacement rate, corresponding to a strain rate,  $\dot{\epsilon}$ , between  $10^{-3}$  and  $10^{-6}$  s $^{-1}$ . Temperatures were varied between 20°C and 800°C at applied confining pressures of 30–300 MPa. Conditions for each experiment are given in Table 1. At the end of each run, force and confining pressure were kept constant during cooling in order to preserve the microfabric and to minimize temperature-induced microcrack development.

**Table 1**  
*Experimental Conditions*

Sample no.	$P_c$ (MPa)	$T$ (°C)	$\dot{\epsilon}$ (s <sup>-1</sup> )	$\Delta\sigma_{0.05}$ (MPa)	$h_{0.05}$ (MPa)
CM15	100	400	1E-5	198	918
CM17	200	400	1E-5	200	951
CM18	100	400	1E-6	192	756
CM19	100	300	1E-5	205	1,123
CM20	200	300	1E-5	232	1,382
CM21	100	20	1E-4	207	336
CM22	300	20	1E-4	372	1,786
CM23	200	300	1E-6	227	1,294
CM24	200	300	1E-4	229	1,199
CM26	200	200	1E-5	238	1,345
CM27	100	400	1E-4	212	1,027
CM28	300	300	1E-5	227	1,309
CM29	100	300	1E-6	227	1,169
CM30	300	400	1E-5	209	945
CM31/38	200	400	1E-6	205	734
CM32	200	400	1E-4	211	1,125
CM33	300	400	1E-4	220	1,150
CM34	300	200	1E-4	245	1,450
CM35	100	300	1E-4	209	1,029
CM36/25	300	300	1E-4	227	1,290
CM37	100	300	1E-5	215	1,074
CM39	300	200	1E-6	239	1,411
CM40	100	200	1E-4	234	1,068
CM41	200	200	1E-4	240	1,399
CM42	300	200	1E-5	243	1,435
CM43	200	200	1E-6	233	1,293
CM44	100	200	1E-5	217	987
CM45	100	200	1E-6	227	1,165
CM46	300	300	1E-6	239	1,249
CM47	300	400	1E-6	211	641
CM55	100	600	1E-4	124	173
CM57	300	600	1E-5	113	87
CM58	300	600	1E-6	91	57
CM59	200	600	1E-5	112	89
CM60	100	600	1E-5	106	146
CM61	200	600	1E-4	134	135
CM62	200	600	1E-6	89	79
CM63	100	600	1E-6	89	71
CM65	300	600	1E-4	143	193
CM66	300	800	1E-4	44	38
CM67	100	800	1E-4	42	50
CM68	200	800	1E-4	44	23
CM69	300	700	1E-4	79	40

**Table 1**  
*Continued*

Sample no.	$P_C$ (MPa)	$T$ (°C)	$\dot{\epsilon}$ (s <sup>-1</sup> )	$\Delta\sigma_{0.05}$ (MPa)	$h_{0.05}$ (MPa)
CM70	100	700	1E-4	77	83
CM71	100	700	1E-3	89	154
CM72	50	700	1E-4	71	111
CM73	300	700	1E-3	104	176
CM74	100	650	1E-4	97	90
CM75	300	650	1E-4	103	69
CM76	300	650	1E-5	81	98
CM77	100	650	1E-5	81	74
CM78	50	800	1E-4	39	80
CM79	100	800	1E-3	61	143
CM80	300	800	1E-3	60	109
CM81	100	20	1E-6	271	822
CM82	300	20	1E-6	345	1,950
CM83	150	300	1E-5	185	1,218
CM84	30	20	1E-5	157	-705
CM85	150	20	1E-5	307	948
CM86	50	20	1E-5	203	-294
CM87	30	300	1E-5	144	364
CM88	30	600	1E-5	85	126
CM89	100	20	1E-5	275	557
CM90	50	300	1E-5	175	686
CM91	30	400	1E-5	136	487
Mb24	100	120	5E-5	255	1,538
Mb28	200	20	5E-4	372	1,387
Mb32	400	20	5E-5	400	1,729
Mb37	200	20	1E-5	335	1,080
Mb40	200	20	1E-6	303	1,519
Mb43	200	20	5E-6	323	1,630
Mb58	200	120	5E-5	300	1,866
Mb60	100	360	5E-5	211	975
Mb61	300	120	5E-5	306	1,926
Mb75	30	20	5E-5	-	-
Mb76/36	300	20	1E-4	401	1,584
Mb77	400	20	1E-4	414	1,612
Mb79/78	300	20	5E-5	391	2,025
Mb80	100	20	1E-4	265	169
Mb84	200	20	5E-5	346	1,739
Mb85	200	20	1E-4	357	1,729
Mb86	30	20	1E-4	-	-
Mb90	30	120	5E-5	147	-181
Mb92	100	20	5E-5	273	802
Mb93	300	240	5E-5	288	3,004
Mb96	100	240	5E-5	227	1,092
Mb97	200	360	5E-5	245	2,107



**Table 1**  
*Continued*

Sample no.	$P_C$ (MPa)	$T$ (°C)	$\dot{\epsilon}$ (s <sup>-1</sup> )	$\Delta\sigma_{0.05}$ (MPa)	$h_{0.05}$ (MPa)
Mb98	30	240	5E-5	164	542
Mb99	200	240	5E-5	269	2,283
Mb104	30	360	5E-5	158	584
Mb111	300	360	5E-5	235	2,466

For comparison, we also include the results of a different suite of tests on Carrara marble obtained in a different deformation apparatus at strain rates of  $5 \times 10^{-5}$  and  $1 \times 10^{-4}$  s<sup>-1</sup>, pressures of 30–400 MPa, and temperatures between 20 and 360°C (Rybacki, 1986). These experiments, denoted as Mbxx, were done on dry cylindrical samples of 30 mm diameter and 60 mm length up to strains of about 0.06 in two separate apparatuses. Room temperature tests were performed on rubber-jacketed samples using a servo-hydraulically driven deformation apparatus (Rummel, 1975). The oil confining pressure medium allowed volumetric strain to be obtained by measuring the oil volume displaced during deformation at constant confining pressure (accuracy  $\leq 0.1\%$ ) (Gowd & Rummel, 1980). Experiments at temperatures up to 360°C were done with a second deformation apparatus using Argon gas as confining pressure medium and aluminum jackets 0.5 mm thick (Alheid, 1981). In both test series, axial  $P$ -wave velocities were recorded every 3–30 s using piezoelectric transducers (Rummel, 1975). Several measurements were stacked to improve the signal/noise ratio. At temperatures  $>20^\circ\text{C}$  depolarization of the ultrasonic transducers (Valvo, PXE-5, Curie temperature: 285°C) of up to about 20% at  $T = 210^\circ\text{C}$  occurred, preventing successful measurements at high  $T$  ( $>250^\circ\text{C}$ ).

Qualitative observations of the optical microstructures were done on polished thin sections of selected samples, usually oriented parallel to the long axis of the sample. SEM observations were used to identify microcracks. To increase contrast, some of the samples were saturated with low-viscosity epoxy enriched with strontianite. The best results in terms of detailed and improved inspection were obtained using a FEI Quanta 3D FEG dual-beam SEM at GFZ, in backscattering mode. SEM samples were made from polished thick sections taken parallel to the long cylinder axis. Dislocation structures of selected samples were imaged using selected area diffraction (SAD) observations in one of two transmission electron microscopes (JEOL 200CX or 2000FX at MIT). In the TEM examinations, specimen sections were oriented perpendicular to the long cylinder axis and thinned using an argon ion beam.

### 3. Results

#### 3.1. General Summary of Mechanical Behavior

A total of 67 CMxx tests were performed in the Paterson apparatus at the GeoForschung Zentrum, Potsdam, Germany. Three of these experiments had repeated conditions; six additional “annealing” experiments with no axial loading were also done. We also report results of 28 experiments done by Rybacki (1986) in two other deformation apparatuses at the Ruhr-University Bochum, Germany. One machine used fluid as the confining medium and the second used gas. These tests were done on larger samples (Mbxx), and include two tests with repeated conditions (Table 1). The bulk of our experiments (CMxx) were done with a consistent technique on a single mechanical apparatus, and with systematic variations of  $T$ ,  $P_C$ , and  $\dot{\epsilon}$ . Thus, these test results facilitate comparisons amongst the various conditions. We characterized each stress-strain curve using two separate, but related, aspects: the differential stress,  $\Delta\sigma$ , and the hardening coefficient,  $h$ . Typical curves for  $\Delta\sigma$  and  $h$  vs.  $\epsilon$  obtained at room (20°C), low (200°C), intermediate (400°C) and high (600°C) temperatures are shown in Figure 2. The stress-strain curves (Figures 1, 2a, 2c, 2e and 2g) are generally consistent with previous studies (e.g., Edmond & Paterson, 1972; Fredrich et al., 1989; Rutter, 1974).

Macroscopically, at all conditions, deformation was ductile over the observed  $\epsilon < 0.12$ , that is, inelastic strains of up to 0.12 were achieved without localized rupture. However, we note that samples deformed at  $T = 20^\circ\text{C}$  and  $P_C < 100$  MPa exhibited strain weakening ( $h < 0$ ). In almost all other conditions, the samples showed continuous, non-linear hardening without reaching steady state up to the highest applied strain. Both  $\Delta\sigma$  and  $h$  are unique functions of strain that vary differently with changes in  $T$ ,  $P_C$ , and  $\dot{\epsilon}$ . For example, at  $T = 200^\circ\text{C}$ ,  $\Delta\sigma$  for  $\epsilon = 0.11$

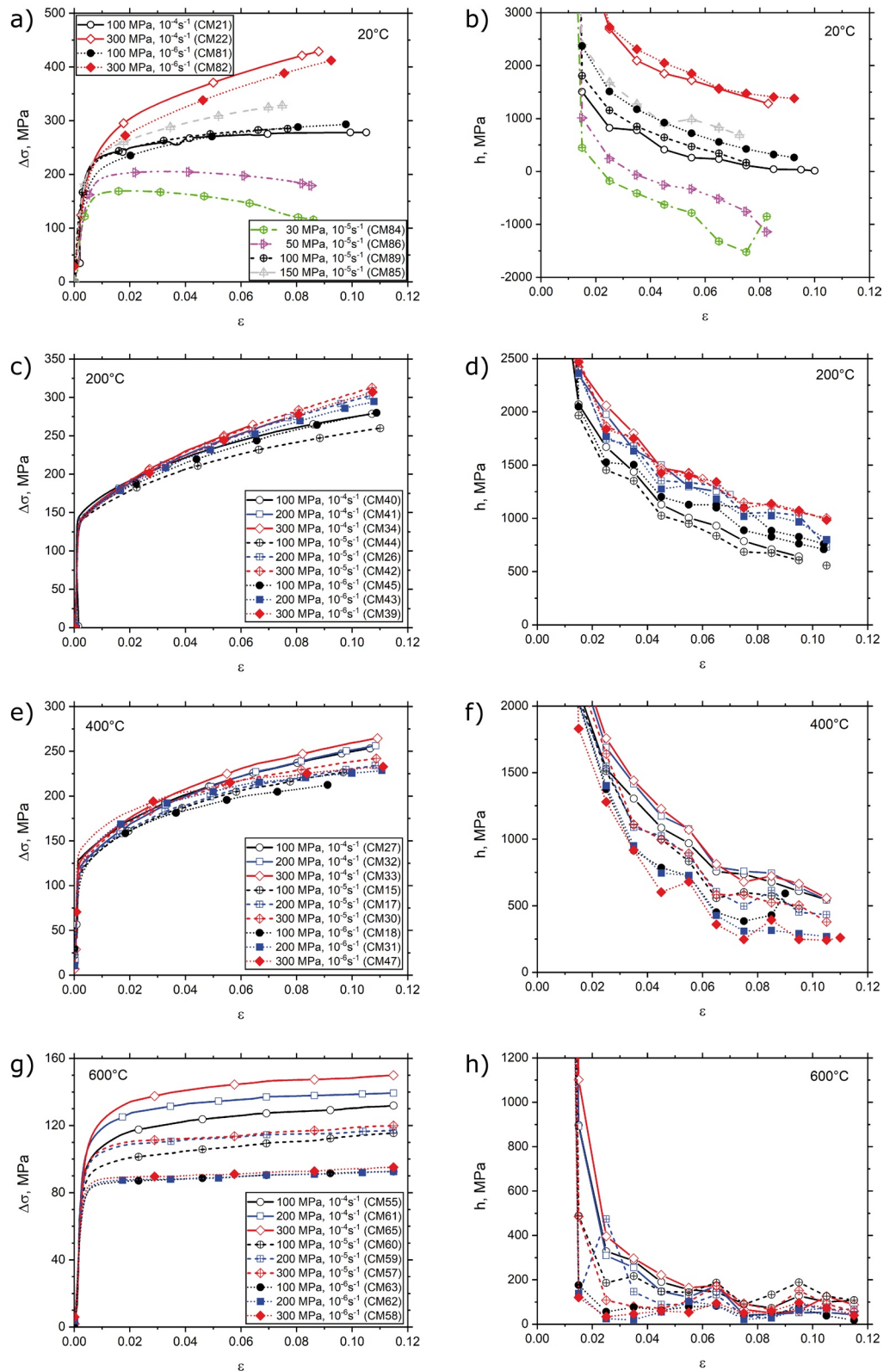


**Figure 2.** Selected curves of stress vs. strain (a, c, e, g) and hardening coefficient vs. strain (b, d, f, h) at  $T = 20^\circ\text{C}$  (a, b),  $200^\circ\text{C}$  (c, d),  $400^\circ\text{C}$  (e, f), and  $600^\circ\text{C}$  (g, h). At  $20^\circ\text{C}$  and  $P_C < 100$  MPa, samples show strain weakening, that is, negative  $h$ . At all other conditions  $h$  is positive. The influence of pressure on the deformation behavior is most significant at  $T = 20^\circ\text{C}$ . The values of  $P_C$  and  $\dot{\epsilon}$  are given in the legend for each curve.



is  $\approx 25\%$  higher than that for  $\epsilon = 0.05$ ; at  $T = 600^\circ\text{C}$ , strength increases by  $\approx 6\%$  over the same strain interval. Similarly, over that strain interval,  $h$  decreases by about 27% at  $200^\circ\text{C}$  and 54% at  $600^\circ\text{C}$ .

In general, for fixed  $\dot{\epsilon}$  and  $T < 700^\circ\text{C}$ , the stress at a given  $\epsilon$ ,  $\Delta\sigma(\epsilon)$ , is usually greater when  $P_c$  increases (Figure 2). Likely, this behavior indicates that some dilatant processes are occurring. In addition, when the other variables are fixed, stresses typically have lower values when  $T$  increases or when  $\dot{\epsilon}$  decreases, suggesting that some crystal-plastic deformation processes are also operating. It is important to notice the changes in the curves of  $\Delta\sigma(\epsilon)$  are complex functions of  $T$ ,  $P_c$ , and  $\dot{\epsilon}$ . As expected, the pressure-sensitivity of stress at a given strain tends to decrease with decreasing  $\dot{\epsilon}$  and increasing  $T$ . For example, curves of  $\Delta\sigma(\epsilon)$  are nearly independent of  $P_c$  when  $T = 600^\circ\text{C}$  and  $\dot{\epsilon} = 10^{-6} \text{ s}^{-1}$  (Figure 2g), but they increase with  $P_c$  in the temperature range  $20\text{--}400^\circ\text{C}$  (Figures 2a, 2c and 2e). At  $20^\circ\text{C}$ , curves of the hardening coefficients vs. strain,  $h(\epsilon)$  are pressure-dependent (Figure 2b). At  $200^\circ\text{C}$ , curves of  $h(\epsilon)$  for a given strain rate still depend on  $P_c$ , but the variation is much smaller (Figure 2d), whereas at  $400^\circ\text{C}$  the influence of strain rate on the hardening coefficients is larger than of pressure (Figure 2f). At  $600^\circ\text{C}$ , the sensitivity of  $h(\epsilon)$  to  $P_c$  is small and  $h$  falls to very low values with increasing strain (Figure 2h).

To simplify the visualization of the mechanical behavior, we compare values of  $\Delta\sigma$  and  $h$  measured at fixed  $\epsilon = 0.05$  over the entire set of conditions of  $T$ ,  $P_c$ , and  $\dot{\epsilon}$  (Figures 3–5). This construct reduces the curves of  $\Delta\sigma(\epsilon)$  and  $h(\epsilon)$  to a single, representative value, denoted  $\Delta\sigma_{0.05}$  or  $h_{0.05}$  respectively, where  $\Delta\sigma_{0.05}$  is defined here as the sample strength at  $\epsilon = 0.05$ . Over all the conditions,  $\Delta\sigma_{0.05}$  varies between 39 and 414 MPa, whereas  $h_{0.05}$  varies between  $-700$  to 3,000 MPa (Table 1).

### 3.1.1. Variations of $\Delta\sigma_{0.05}$ and $h_{0.05}$ at Fixed $T$ and $\dot{\epsilon}$ , but Differing $P_c$

The evolution of  $\Delta\sigma_{0.05}$  and  $h_{0.05}$  with increasing pressure at  $20^\circ\text{C}$  is shown in Figures 3a and 3b, respectively. Data from Edmond and Paterson (1972) (EP), Rutter (1974) (RUT) and Fredrich et al. (1989) (FEW) are also shown. Except at a strain rate of  $10^{-4} \text{ s}^{-1}$ , data from different studies agree well, although the scatter for  $h_{0.05}$  is larger than that for  $\Delta\sigma_{0.05}$ . Data from the MBxx tests and Edmond and Paterson (1972) indicate that strength changes very slowly at high  $P_c$  ( $\gtrsim 500$  MPa). At  $20^\circ\text{C}$ ,  $h_{0.05}$  varies strongly with  $P_c$  when  $P_c < 400$  MPa. In fact, when  $P_c \lesssim 100$  MPa,  $h_{0.05}$  is small, and, in some cases, negative (Figure 3b). As noted above, both parameters increase non-linearly with  $P_c$ , and approach constant values at  $P_c \approx 500$  MPa.

The evolution of  $\Delta\sigma_{0.05}$  with pressure for a strain rate of  $10^{-5} \text{ s}^{-1}$  and various fixed temperatures is shown in Figure 3c. Strength shows the greatest sensitivity to  $P_c$  at room  $T$ , increasing non-linearly from 150 MPa at  $P_c = 30$  MPa to over 300 MPa at  $P_c = 200$  MPa. In the temperature range of  $200\text{--}400^\circ\text{C}$ ,  $\Delta\sigma_{0.05}$  is less dependent on  $P_c$  than at room  $T$ . For example, at  $T = 200^\circ\text{C}$ ,  $\Delta\sigma_{0.05}$  increases by only 5% over the interval of  $100 \text{ MPa} < P_c < 200 \text{ MPa}$ , whereas it increased by 20% over the same interval at room  $T$ . At  $T = 300\text{--}400^\circ\text{C}$ , the absolute values of  $\Delta\sigma_{0.05}$  at each pressure are less for increased  $T$ , but the rate of increase of  $\Delta\sigma_{0.05}$  with pressure is similar to that at  $200^\circ\text{C}$ .  $\Delta\sigma_{0.05}$  changes only very slowly at  $600^\circ\text{C}$ . For a fixed strain rate of  $10^{-5} \text{ s}^{-1}$ ,  $h_{0.05}$  also depends on pressure non-linearly at the different temperatures (Figure 3d). In general, the rate of change of  $h_{0.05}$  with increasing pressure is smaller as  $T$  increases, becoming very small at  $T \geq 600^\circ\text{C}$  (Figure 3d). At room  $T$ ,  $h_{0.05}$  increases by 50% over the pressure range of  $100\text{--}150$  MPa, whereas at  $600^\circ\text{C}$  and above, the pressure sensitivity of hardening is zero or slightly negative.

### 3.1.2. Variations of $\Delta\sigma_{0.05}$ and $h_{0.05}$ at Fixed $P_c$ and $T$ , but Differing $\dot{\epsilon}$

The variation of strength and hardening coefficients at  $\epsilon = 0.05$  with changes in strain rate are shown in Figure 4 for various  $T$ . The data for Figures 4a–4c were taken with  $P_c$  fixed at 300 MPa; those in Figure 4d were done with  $P_c = 150$  MPa (Notice that Figures 4a, 4b and 4d have semilogarithmic scale; while Figure 4c has full-logarithmic scale.) At  $T \geq 600^\circ\text{C}$  and  $P_c = 300$  MPa,  $\Delta\sigma_{0.05}$  generally increases with increasing strain rate, but at lower temperatures and the same  $P_c$ , the sensitivity of  $\Delta\sigma_{0.05}$  to  $\dot{\epsilon}$  is much less (Figures 4a and 4c).

For comparison, we consider two generic relationships between  $\Delta\sigma$  and  $\dot{\epsilon}$ , the first, an exponential relation between stress and strain rate, and the second, a power-law relation (Figures 4a and 4c). If strain rate is related exponentially to stress then

$$\dot{\epsilon} \sim \exp(\Delta\sigma/\sigma_0) \quad (1)$$

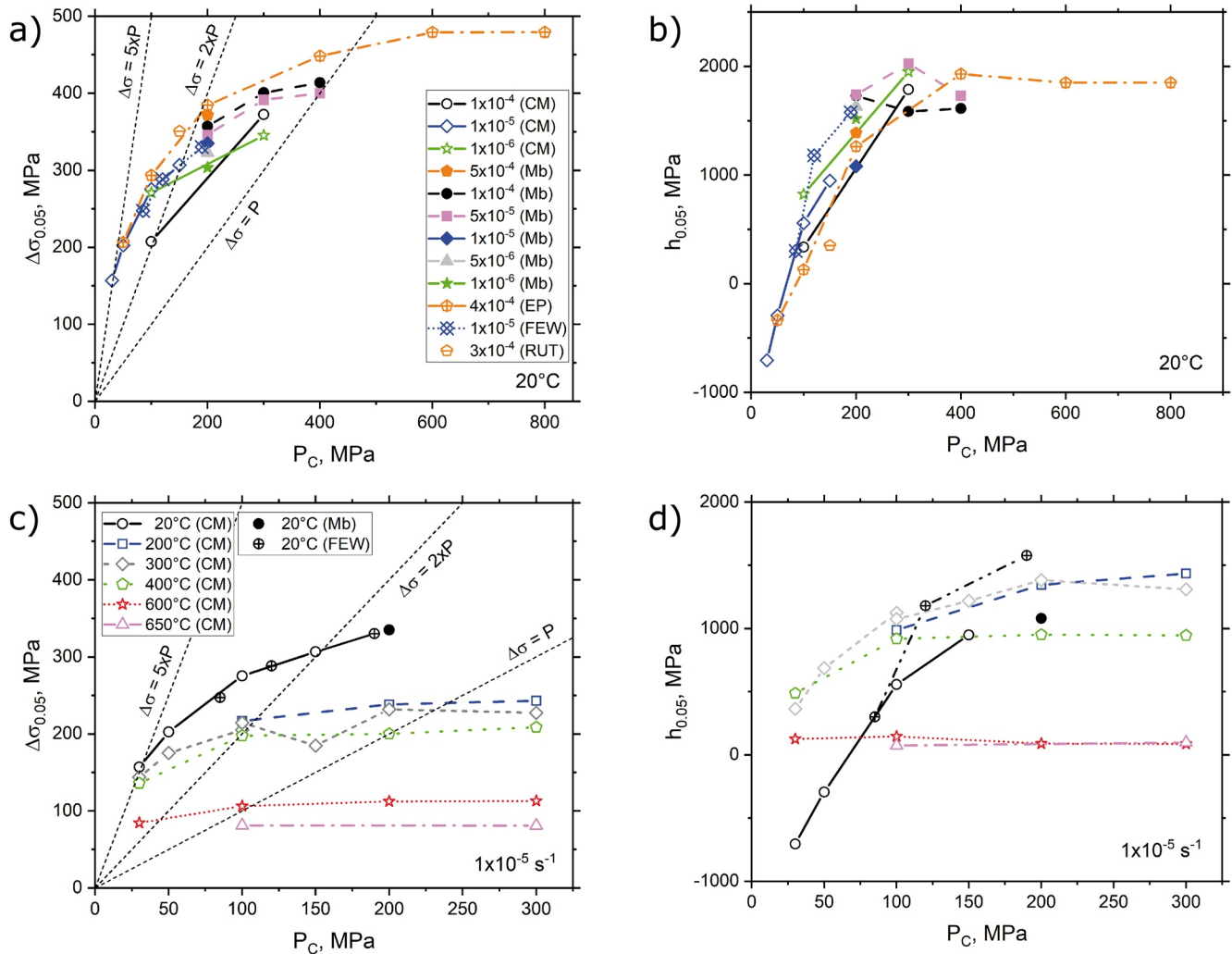


**Figure 3.** Strength (a) and hardening coefficient (b) at strain of 0.05 vs. pressure at  $T = 20^\circ\text{C}$ . At room temperature, high pressures are required to achieve pressure-independent strength and hardening coefficient. Strength (c) and hardening coefficient (d) at strain of 0.05 vs.  $P_c$  at  $\dot{\epsilon} = 1 \times 10^{-5} \text{ s}^{-1}$  and different fixed temperatures. At a given strain rate, the pressure-sensitivities of both  $\Delta\sigma_{0.05}$  and  $h_{0.05}$  decrease with increasing temperature. Thin broken lines indicate different ratios of differential strength vs. confinement. EP are data from Edmond and Paterson (1972), FEW from Fredrich et al. (1989) and RUT from Rutter (1974).

The normalization stresses  $\sigma_0$  found from fits to the data vary between 1.3 at  $200^\circ\text{C}$  to 11.3 MPa at  $T = 600^\circ\text{C}$ , where rate dependence is maximum (Figure 4a). In the temperature range of  $200\text{--}400^\circ\text{C}$ ,  $\Delta\sigma_{0.05}$  depends only weakly on strain rate. At room temperature,  $\Delta\sigma_{0.05}$ , once again, is positively correlated with increasing  $\dot{\epsilon}$ , but less strongly than at high  $T$ . Alternatively, at high temperatures, it is common to relate the strain-rate sensitivity of stress as a power-law with exponent  $n$  (Karato, 2008) (Figure 4c):

$$\dot{\epsilon} \sim \Delta\sigma^n \quad (2)$$

Note that the linear regression lines shown in the figure are proportional to  $1/n$ . Values for  $n$  at high  $T$  vary between 7.7 at  $T = 800^\circ\text{C}$  to 10.1 at  $600^\circ\text{C}$ , similar to those found in previous laboratory studies (e.g., Pieri, Burlini, et al., 2001; Schmid et al., 1980). For both models, in the intermediate temperature range of  $200\text{--}400^\circ\text{C}$ ,  $\Delta\sigma_{0.05}$  is almost independent of strain rate. Hence,  $n$  is very large and variable. At  $T = 20^\circ\text{C}$ ,  $n$  is smaller than at intermediate  $T$ , (30–60), but larger than at high  $T$ .

In contrast to strength, hardening coefficients,  $h_{0.05}$ , at  $T = 20^\circ\text{C}$  decrease with increasing  $\dot{\epsilon}$  for both  $P_c = 300 \text{ MPa}$  (Figure 4b) and  $P_c = 150 \text{ MPa}$  (Figure 4d). For all other temperatures,  $h_{0.05}$  increases with strain rate, but the

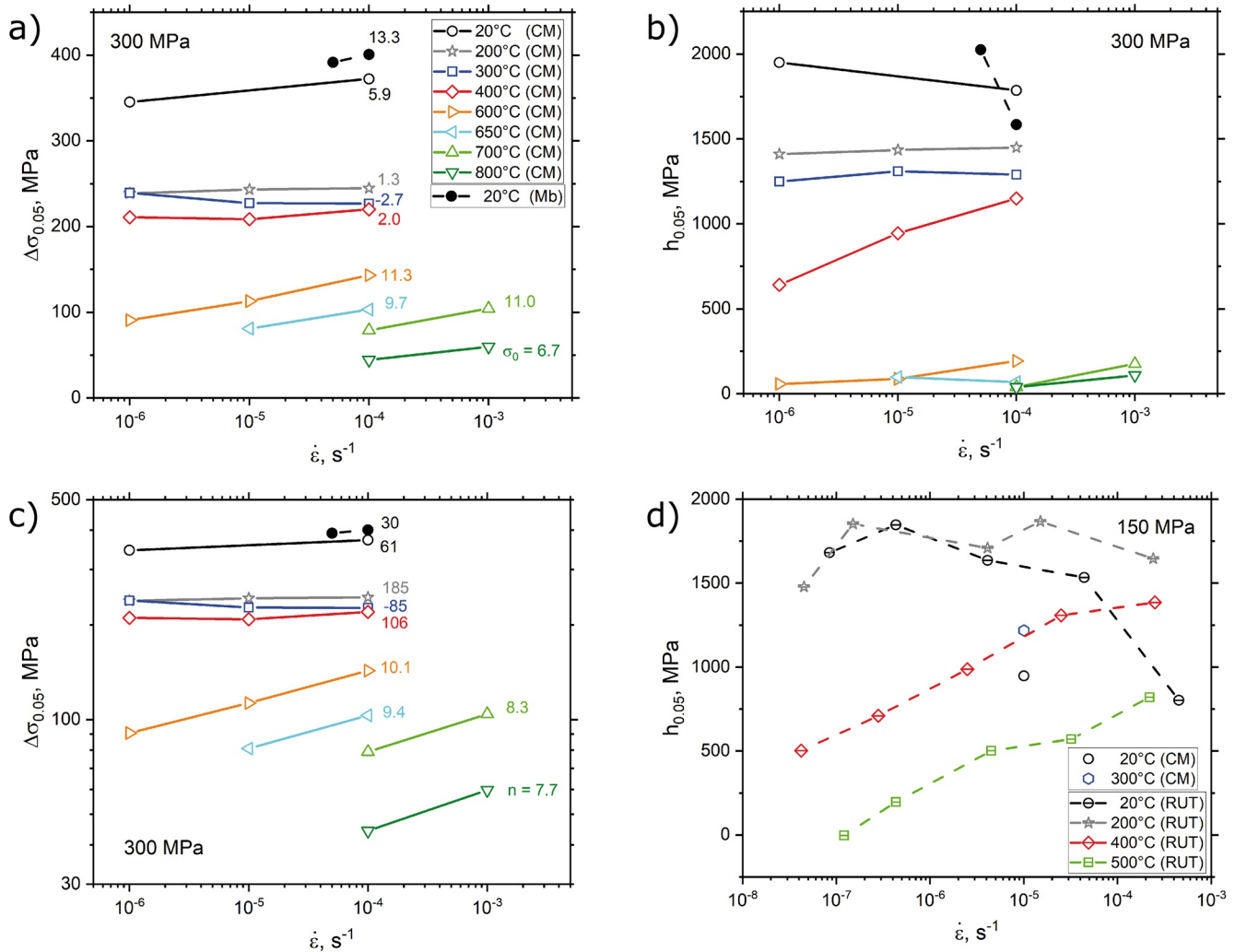


**Figure 4.** Strength (a, c) and hardening coefficient (b, d) at 0.05 strain vs. strain rate, determined at various temperatures and 300 MPa pressure (a–c), as well as at 150 MPa pressure (d). Note a minor strain rate sensitivity at temperatures between 200 and 400°C.  $\sigma_0$  in (a) and  $n$  in (c) denote the normalization stress and stress exponent assuming an exponential and power law relationship between stress and strain rate, respectively, see text for details. RUT are data from Rutter (1974).

increases are weakest in the range  $T = 200\text{--}300^\circ\text{C}$ . Temperature sensitivity of  $h_{0.05}$  is highest at  $T = 400\text{--}500^\circ\text{C}$  but is low again at  $T \geq 600^\circ\text{C}$ .

### 3.1.3. Variations of $\Delta\sigma_{0.05}$ and $h_{0.05}$ at Fixed $P_c$ and $\dot{\epsilon}$ , but Differing $T$

The influence of temperature on  $\Delta\sigma_{0.05}$  and  $h_{0.05}$  for given  $P_c$  when  $\dot{\epsilon} = 10^{-5} \text{ s}^{-1}$ , is shown in Figures 5a and 5b. At this strain rate,  $\Delta\sigma_{0.05}$  decreases non-linearly with increasing  $T$  for all  $P_c$ , but at lower rates when  $P_c < 100 \text{ MPa}$  (Figure 5a). The sensitivity of strength to  $T$  increases when  $T > 300^\circ\text{C}$  for all  $P_c$ . At  $\dot{\epsilon} = 10^{-5} \text{ s}^{-1}$ , the hardening coefficients,  $h_{0.05}$ , also show a unique relationship with  $T$  (Figure 5b). Values for  $h_{0.05}$  are maximum in the range  $200 < T < 400^\circ\text{C}$ . Below that temperature range,  $h_{0.05}$  increases with  $T$  if pressures are 200 MPa and below. When  $T = 20^\circ\text{C}$ ,  $h_{0.05}$  may even be negative for  $P_c < 100 \text{ MPa}$ .

The changes in  $\Delta\sigma_{0.05}$  with changing  $T$ , when pressure is fixed at 100 MPa, and for various fixed strain rates are shown in Figure 5c. At room  $T$ ,  $\Delta\sigma_{0.05}$  is lowest when  $\dot{\epsilon} = 10^{-4} \text{ s}^{-1}$ , that is, the fastest strain rate. When  $T$  is  $200\text{--}300^\circ\text{C}$ , the variation in  $\Delta\sigma_{0.05}$  with changing strain rate is apparently within the error of measurement. Above  $300^\circ\text{C}$ ,  $\Delta\sigma_{0.05}$  depends inversely on  $\dot{\epsilon}$ . Similarly, when  $P = 100 \text{ MPa}$ ,  $h_{0.05}$  depends negatively on  $\dot{\epsilon}$  when  $T = 20^\circ\text{C}$  (Figure 5d). Values for  $h_{0.05}$  reach a plateau at  $200\text{--}300^\circ\text{C}$ , and then decrease with increasing  $T$ . When  $T > 300^\circ\text{C}$ ,  $h_{0.05}$ , at a given  $T$ , decreases with decreasing  $\dot{\epsilon}$ .

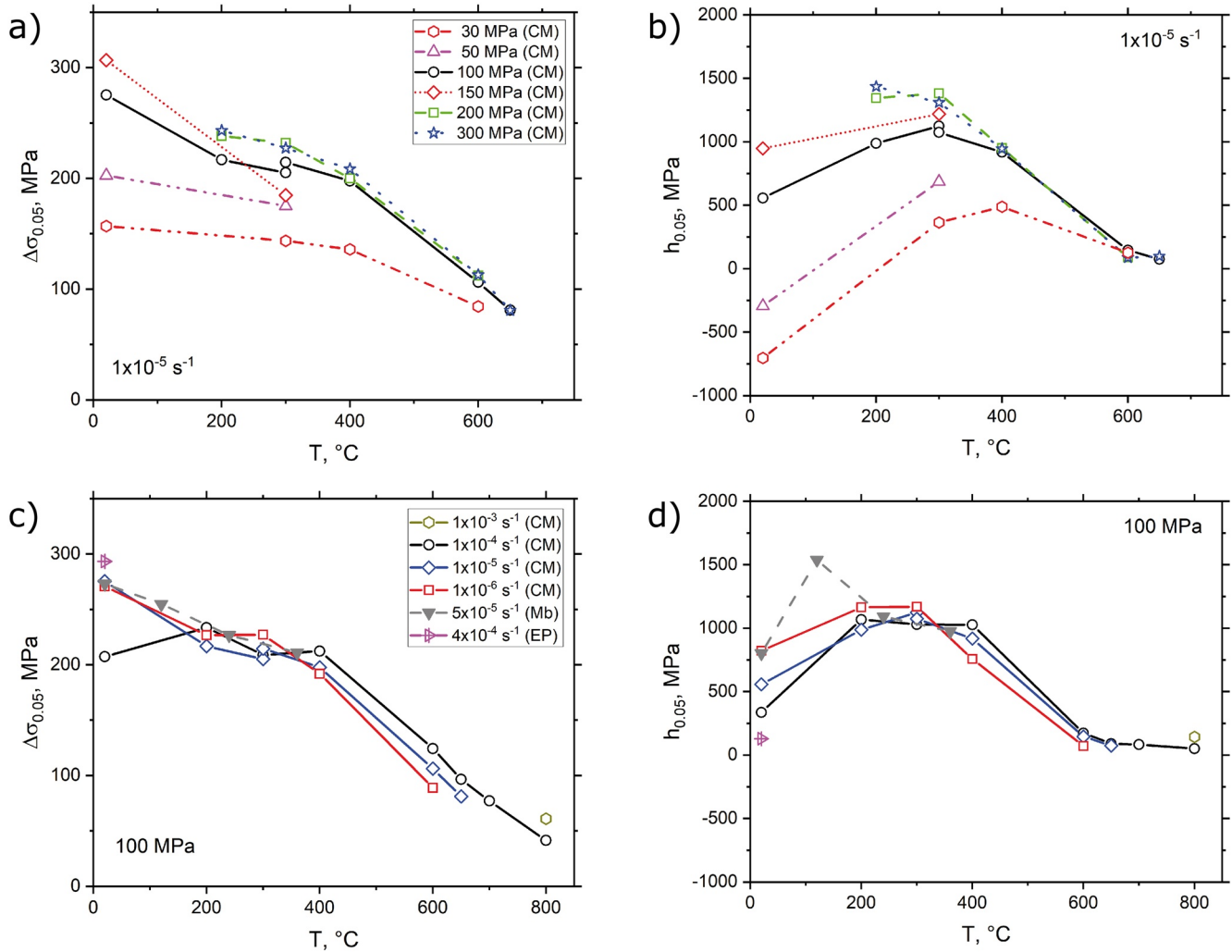


**Figure 5.** Variation of strength (a) and hardening coefficient (b) at  $\epsilon = 0.05$  vs. temperature at fixed strain rate of  $\dot{\epsilon} = 1 \times 10^{-5} \text{ s}^{-1}$  and different pressures. Variation of  $\Delta\sigma_{0.05}$  and  $h_{0.05}$  with  $T$ , when  $P_c = 100 \text{ MPa}$  and at various strain rates (c, d, respectively). In all cases,  $\Delta\sigma_{0.05}$  and  $h_{0.05}$  are relatively independent of  $T$  in the range between about 200 to 400°C. EP are data from Edmond and Paterson (1972).

### 3.1.4. Volumetric Strain and Variations of Axial Ultrasonic *P*-Wave Velocities

For some of the Mbxx samples, ultrasonic *P*-wave velocities in axial direction and volumetric strain were recorded during deformation (Rybacki, 1986). For samples deformed at room temperature and  $\dot{\epsilon} = 5 \times 10^{-5} \text{ s}^{-1}$ , there is a transition from strain weakening at  $P_c = 30 \text{ MPa}$  to strain hardening at  $P_c = 100 \text{ MPa}$  and above (Figures 6a and 6b). After yielding, the volumetric strain,  $\epsilon_v$ , turns from initial compaction to dilatant behavior at 30 MPa confining pressure and after about axial strain of 0.01 also at  $P_c = 100 \text{ MPa}$  (Figure 6c), although hardening is still positive. At  $P_c = 200 \text{ MPa}$ ,  $\epsilon_v$  remains almost constant with increasing strain. At higher confining pressure a slight ongoing compaction is observed, probably caused by the progressive closure of open fractures at grain boundaries. Note that the volumetric strain shown here is not measured using strain gauges, which are local measurements. Rather, the volumetric strains are calculated from the amount of oil confining-pressure medium added or removed to keep the pressure constant during deformation, and therefore, measure volumetric strain of the bulk sample. In the dilatant regime (low  $P_c$ ), the relative change of axial velocity,  $\Delta V_p/V_{p0}$ , that is, the change of axial velocity,  $\Delta V_p$ , normalized by the initial velocity after applying  $P_c$ ,  $V_{p0}$ , is reduced, depending on the magnitude of  $P_c$  (Figure 6d). At pressures  $\geq 200 \text{ MPa}$ , where compaction prevails,  $\Delta V_p/V_{p0}$  increases uniformly up to axial strain of 0.06. These results suggest that velocity measurements are very sensitive to volume changes during deformation, even though measurements were done parallel to the loading direction, where mainly axial cracks are expected to form.

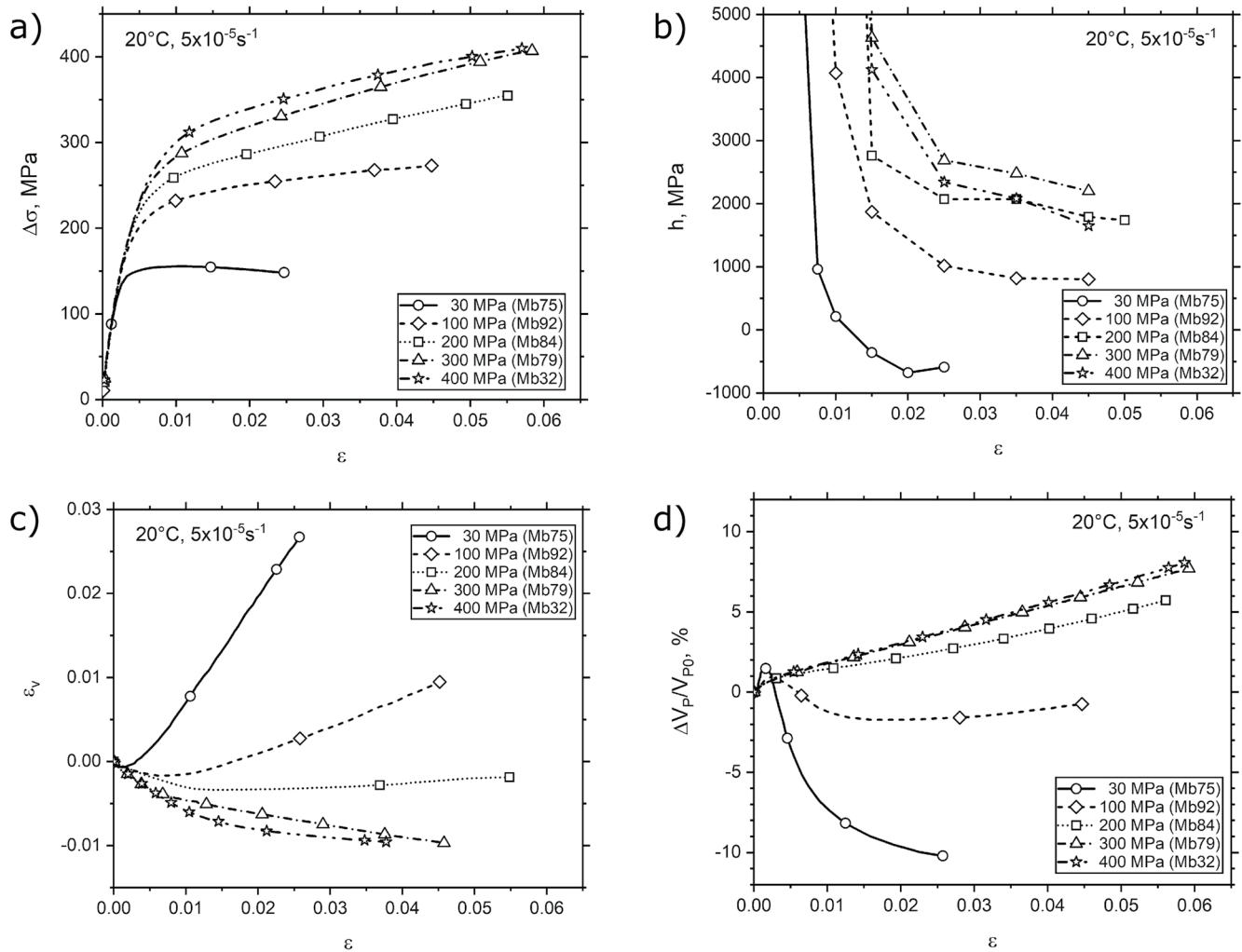


**Figure 6.** Stress-strain curves (a), hardening coefficient-strain curves (b), and evolution of volumetric strain (c) and relative change of axial  $P$ -wave velocity (d) with axial strain of Mbxx samples deformed at different pressures and  $T = 20^\circ\text{C}$ ,  $\dot{\epsilon} = 5 \times 10^{-5} \text{ s}^{-1}$ . Note that at low pressure samples exhibit strain weakening with negative  $h$ , accompanied by dilatant behavior and strong velocity reduction.

Stress-strain curves of MBxx samples deformed at similar strain rate, confining pressures between 30 and 300 MPa, and  $T = 120^\circ\text{C}$  and  $240^\circ\text{C}$ , are shown in Figures 7a and 7b, respectively. Pressure sensitive strain hardening is evident for all the tests, except for the sample deformed to high strain at  $T = 120^\circ\text{C}$  and  $P_c = 30 \text{ MPa}$  (Figures 7c and 7d). The associated relative  $P$ -wave velocity change is negative at  $P_c = 30 \text{ MPa}$  and  $T = 120^\circ\text{C}$ , but positive for all other samples (Figures 7e and 7f). These velocity reductions are measured at low  $T$  ( $\leq 150^\circ\text{C}$ ) and  $P_c$  ( $\leq 100 \text{ MPa}$ ), that is, conditions under which strain weakening is observed. We infer that cataclastic processes dominate the deformation under these conditions. Note that both stress and hardening of some Mb-samples are higher than those of CM-samples, perhaps related to variations of the starting material or data correction procedures.

### 3.2. Observations of Microstructure

Macroscopically, all deformed samples show barreling without visible macroscopic fractures, except for sample CM84, deformed at the lowest  $P_c$ - $T$  conditions:  $P_c = 30 \text{ MPa}$  and  $T = 20^\circ\text{C}$ . This sample developed localized deformation with shear zones that were a few mm-wide and oriented at about  $30^\circ$  to the sample axis (c.f., Figure S3 in Supporting Information S1). Microscopically, these zones consist of an anastomosing network of thin fractures filled with fine comminuted material. Crack and twin densities increase considerably from the matrix toward the shear zone. At  $P_c = 50 \text{ MPa}$  and  $T = 20^\circ\text{C}$  no macroscopic localization was observed, but inspection



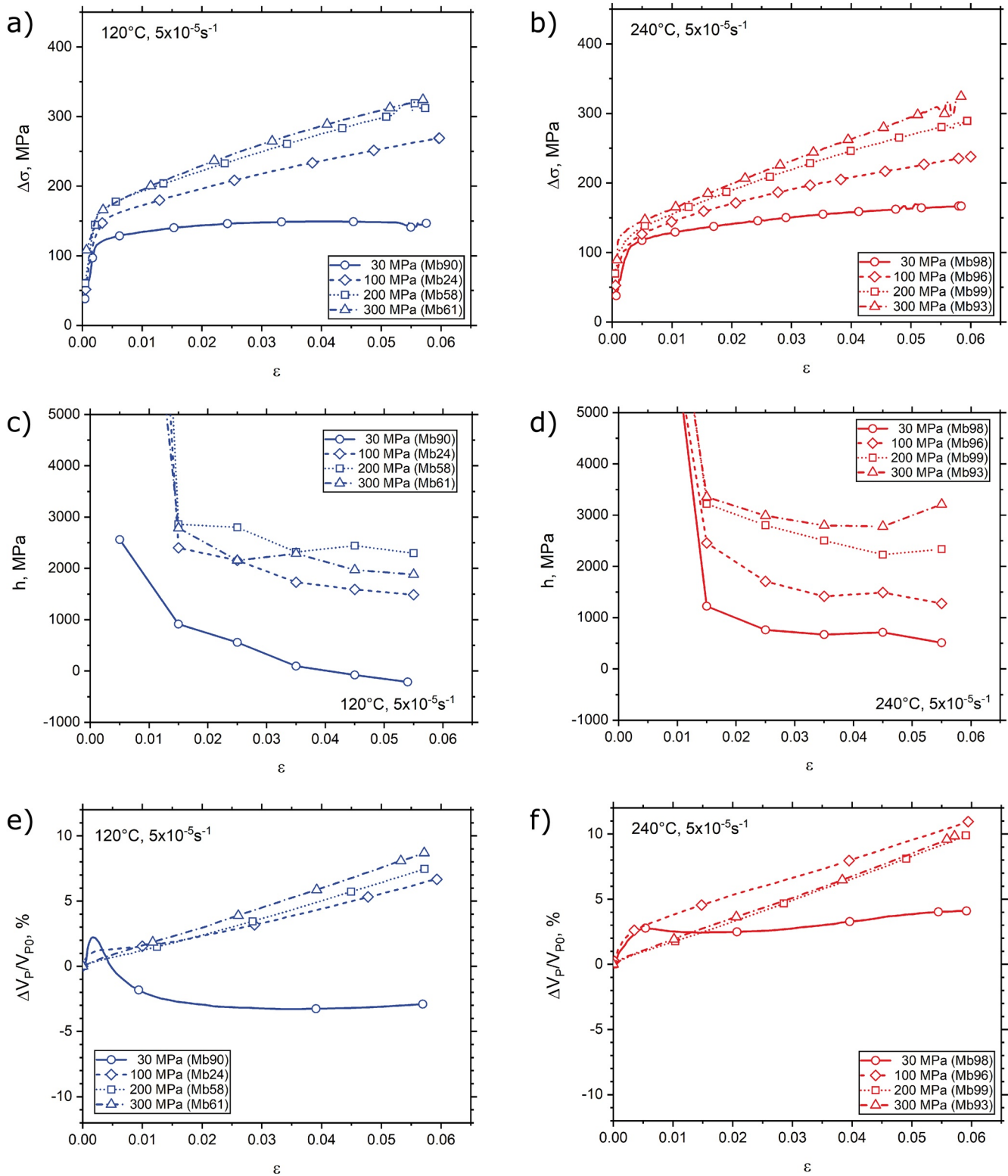


**Figure 7.** Stress-strain curves (a, b), hardening-strain curves (c, d) and relative change of axial ultrasonic  $P$ -wave velocities with strain (e, f) of Mbxx samples deformed at confining pressures between 30 and 300 MPa, strain rate of  $\dot{\epsilon} = 5 \times 10^{-5} \text{ s}^{-1}$  and  $T = 120^\circ\text{C}$  (left column) and  $T = 240^\circ\text{C}$  (right column), respectively. Except at the lowest  $P_c - T$  conditions, stress and hardening increase with pressure, along with continuously increasing  $P$ -wave velocity.



of the thin section still shows a broader zone of intense twinning and microfracturing (Figure 8a). At all other conditions, microstructure is almost homogeneous except for a thin zone close to the top and bottom end of samples with reduced twinning. These features are likely induced by a distortion of the elastic stress distribution due to frictional constraints at the ends.

Optical examinations of thin sections show systematic changes of microstructure as deformation conditions are changed, in particular temperature. From the optical, scanning electron, and transmission electron micrographs (Figures 8 and 9), it is obvious that three main mechanisms operate concurrently at all the conditions reported here: microcracking, twinning, and dislocation formation and motion. It is important to note that the microstructure is slightly affected by heating/cooling and unloading of samples, as verified by inspection of annealed samples under different conditions (c.f., Figure S2 in Supporting Information S1). This effect needs further detailed accounting to provide quantitative assessments of the relative activity of the different mechanisms. Nevertheless, qualitative distinctions in microstructure that depend on applied conditions are evident.

Even at lower  $T$  ( $\lesssim 400^\circ\text{C}$ ), twinning structures show some degree of bending and the terminations of twins at grain boundaries are often spatially correlated with undulatory extinction within the adjacent grain (Figures 8a and 8d). Fractures are apparent along most grain boundaries and as intra-, inter- and transgranular cracks. The intragranular cracks are often collocated with twin boundaries within the same grain or near twin terminations in an adjacent grain (Figures 9b and 9c). Dislocation structures vary spatially and seem to be affected by the presence of twins (Figures 9d and 9e). Although some of these features are also present in iso-statically annealed samples.

Relative activity of the three mechanisms clearly changes with conditions in the deformed samples. In the following, we highlight some qualitative observations, which, although incomplete, give insight into the inter-dependence of the deformation mechanisms. Quantitative determination of the changes in strain partitioning for variations in deformation conditions will require additional observations utilizing statistically robust sampling procedures and EBSD observations. These will be presented in a follow-up paper.

Cataclasis, defined here as the combination of microcracking and granular flow (relative motion of grains or fragments) (e.g., Paterson & Wong, 2005), is present over the entire range of conditions, even at elevated temperatures. Many grain boundaries are fractured, but grain-boundary cracks also occur in samples that have been annealed at pressure and temperature without deformation. These intergranular fractures probably result from the anisotropy of thermal expansion in calcite and, thus, the effect of deformation on grain-boundary cataclasis is obscured. Intra- and transgranular fractures are much less common in the undeformed and annealed samples than in those that have been deformed, and are therefore assumed to have resulted from deformation.

The amount and nature of the cataclasis varies substantially with changes in conditions. In most experiments investigated here, hardening occurred up to the maximum strain. Thus, it is interesting to notice that the cataclastic structure formed at low pressure and temperatures, where strain weakening is observed, is quite distinctive. For example, at  $T = 20^\circ\text{C}$ , when  $P_c = 50$  MPa and  $\dot{\epsilon} = 1 \times 10^{-5} \text{ s}^{-1}$ , granulated material is distributed along grain boundaries and within transgranular fractures (Figure 8a). These bands may extend across several grains. When  $P_c$  is increased to 300 MPa, veins of granulated material are much less common and are not throughgoing. Furthermore, swarms of cracks are generated at grain boundaries, but they do not coalesce to form granulated regions (Figure 8b). Similar swarms are common in experiments when  $20 < T \leq 400^\circ\text{C}$  (Figure 8c). Such features are present, but less common, at higher  $T$ .

Transgranular cracks extending entirely across single grains are often present in experiments when  $T \leq 400^\circ\text{C}$ . There may also be thicker deformation zones oriented parallel to the transgranular fractures. These zones may appear to be secondary twins, but if they are wide enough, individual cleavage rhombs can be resolved inside the deformation zone. Dense networks of fine cleavage fractures may be formed adjacent to grain boundaries (Figures 8d and 9a). Concentrated comminution also occurs within porous regions and fractures may unzip the material from pore-to-pore. Cracks are frequently nucleated from included minerals, large pores, or small grains located at the triple junctions of larger ones.

Twin boundaries may also generate cataclasis. Commonly, intragranular cracks are spatially correlated with larger twins. Small cleavage fractures often cross the twins and form *en echelon* sets (Figures 9b and 9c). Additional fractures can be seen that extend parallel to the twin boundaries. The concurrence sets of parallel and *en echelon*

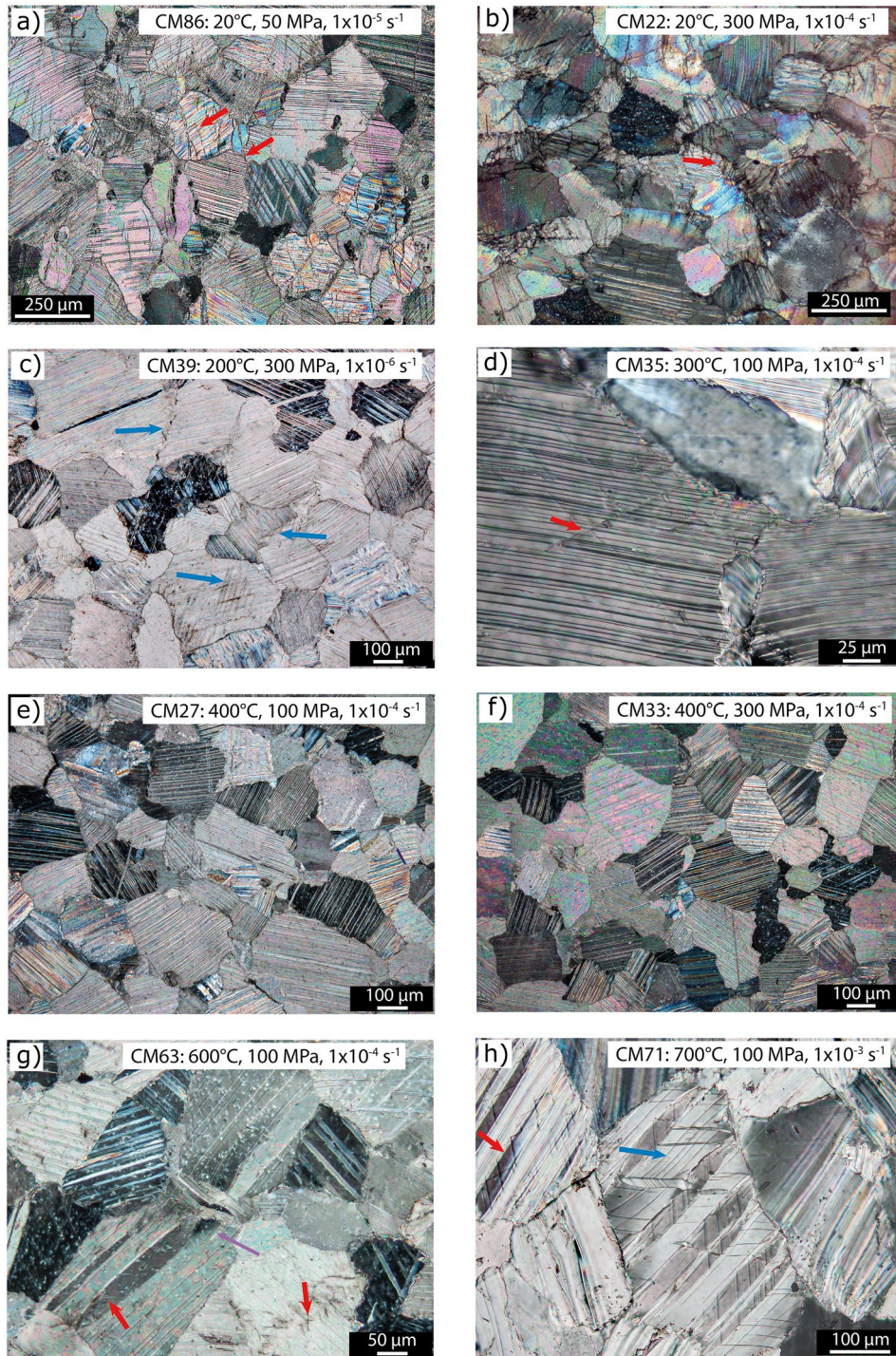


Figure 8.

fractures leads to stair-step structures that could develop into granulated zones within the grain. Fractures that cross lobate twins can be generated even at elevated  $T$  and  $P_c$  (Figure 8g).

TEM micrographs of two samples (CM33, deformed at 200°C,  $P_c = 300 \text{ MPa}$ , and  $\dot{\epsilon} = 10^{-4} \text{ s}^{-1}$ , and CM33, deformed at 400°C,  $P_c = 300 \text{ MPa}$ , and  $\dot{\epsilon} = 10^{-4} \text{ s}^{-1}$ ) demonstrate the interaction of twins and dislocations (Figures 9d and 9e). Note that there are variations in dislocation density both along the trace of the twin boundaries,



as well as perpendicular to the boundaries. When  $T \leq 400^\circ\text{C}$ , dislocation density is spatially quite variable, and the dislocations are tangled, probably indicating that there is limited recovery or cross-slip (Figures 9d and 9e). At  $T = 600^\circ\text{C}$ , some dislocation networks have formed, but the structure is not completely organized into well-formed subgrain networks (Figure 9f). The internal deformation structure also has spatial variations on scales much larger than the TEM micrographs and it is important to acknowledge that the TEM observations are taken over a very small area. Therefore, the limited observations given here may not be completely representative. Notwithstanding this limitation, it is obvious that the interaction between the twin boundaries and dislocations is quite intense.

Twin microstructures are affected most strongly by changing temperature. When  $P_c$  and  $\dot{\epsilon}$  are fixed, both the spacing and thickness of the twins increase with increasing  $T$  (Figure 8). As  $T$  increases, single sets of fine, closely spaced twins, typically formed at  $200\text{--}400^\circ\text{C}$ , are replaced by a combination of thick lobate twins and accompanying features that are either slip lines or thin twins (cf. Figures 8c, 8e and 8h). At higher temperatures, secondary twin sets commonly cross and intersect the primary sets. Cracks may be formed at the intersection of the twin sets, but fractures are less frequent at higher temperatures. Twin bending is more common and is pronounced at high temperatures, although curved twins are present to some degree under all conditions. Terminations of twins at grain boundaries are often associated with twinning in the adjacent grain, boundary offsets, and/or cracking. The influence of changing deformation conditions on the twin volume cannot be determined without additional observations. The detailed effects on twin microstructure when either  $P_c$  or  $\dot{\epsilon}$  are varied independently at fixed  $T$  is also uncertain (Figures 8e and 8f).

Twin densities were counted on selected samples deformed at  $P_c = 300\text{ MPa}$  and  $\dot{\epsilon} = 1 \times 10^{-4}\text{ s}^{-1}$  using optical microscopy and correlated with the stress and hardening coefficient at the maximum strain of about  $\epsilon \approx 0.1$ ,  $\Delta\sigma_{0.1}$  and  $h_{0.1}$ , respectively (Table 2, Figure 10). As seen in Figure 8, optical interference fringes emanating from closely spaced and gently dipping twin boundaries obscure the twin structure, unless the twins are fortuitously oriented perpendicular to the thin section. In addition, slip lines can be produced that might be confused with twin boundaries (Schuster et al., 2019). These slip lines have zone axes that are parallel to the twin boundaries on any observation plane that is cozonal with  $\langle 1\bar{1}210 \rangle$ , and thus, could be counted as a twin boundary. To improve our statistics, we have begun measurements using EBSD techniques, but these are still in progress. Recognizing that there is substantial scatter in the optical determinations, the average twin spacing measured optically was less than  $10\text{ }\mu\text{m}$  at  $T \leq 200^\circ\text{C}$ ; spacings increased up to several tens of micron at higher  $T$ . Since twin density is inversely proportional to twin spacing, the twin densities decrease with increasing  $T$  (Figure 10a). Mean densities range between  $\approx 50$  and  $150$  twins per mm. Since strength decreases with increasing temperature (Figure 5), twin density correlates with increasing strength (Figure 10b). Similarly, low twin densities observed at high  $T$  ( $600\text{--}800^\circ\text{C}$ ) are associated with low hardening coefficients, and the inverse is true at lower  $T$  (Figure 10c).

**Figure 8.** Optical micrographs of deformed samples taken in crossed polarized light. The direction of compression is vertical. (a) Strain weakened sample. Closely spaced, thin twins and both transgranular and grain boundary cracks are common. Numerous zones of crushed rhombs of calcite extend along grain boundaries and within the grains (red arrows), at high angles to the twin planes. Often, the crushed regions extend across several grains. (b) Sample showing continuous strain hardening. Thin, tightly spaced twins are present, along with abundant trans- and intragranular fracturing. Twins are often bent, and undulose extinction is present. Swarms of cracks often extend from the boundaries into the grains (red arrow), but the crushed regions are much less common than at  $P_c = 50\text{ MPa}$ . Note: this section was taken along the radial direction at  $90^\circ$  to the direction of compression. (c) Fine, closely spaced twins are frequent, and some grains have secondary twins. Crack swarms occur both along grain boundaries and within grains (blue arrows). Crushed regions are present but are much less common than at  $T = 20^\circ\text{C}$ . (d) Detailed micrograph of a network of very fine cleavage fractures associated with a fractured grain boundary (red arrow). The fractures within the network are generally at high angles to the twins, but sometimes they deviate as they intersect the twins and extend parallel to the twin boundary. (e) Twin widths and spacings are coarser than those at lower  $T$ . Gently curved twins are largely within primary sets, but a few secondary sets are present. Both inter- and intragranular cracks exist, but intensely granulated regions are not present in this section. (f) Twins are thicker than at lower temperatures, and some are lobate in shape. Intra- and transgranular fractures do exist, but they are not abundant. (g) Thick lobate twins exist, along with thin, fine features that are likely a parallel twin set. The purple arrow marks a region near the termination of a lobate twin that has variable extinction, as does the bent twin in the adjacent grain. Such strain accommodation probably occurs via spatial variations in dislocation density. The larger twins sometimes contain either secondary twins or internal fractures (red arrow). These internal fractures may completely transect the twin or cross from one twin to another. When associated with fractures that run parallel to the twin boundaries, these cracks can form “stair-step” fracture systems. (h) Large lobate twins with variable extinction are common, as are stair-step arrays of fractures (red arrow). Many twins are bounded by cracks. The very thin features (blue arrow) that are parallel to the lobate grains are likely slip lines, but could be also very thin twins or fine fractures. Samples and deformation conditions ( $T\text{--}P_c\text{--}\dot{\epsilon}$ ) are indicated.

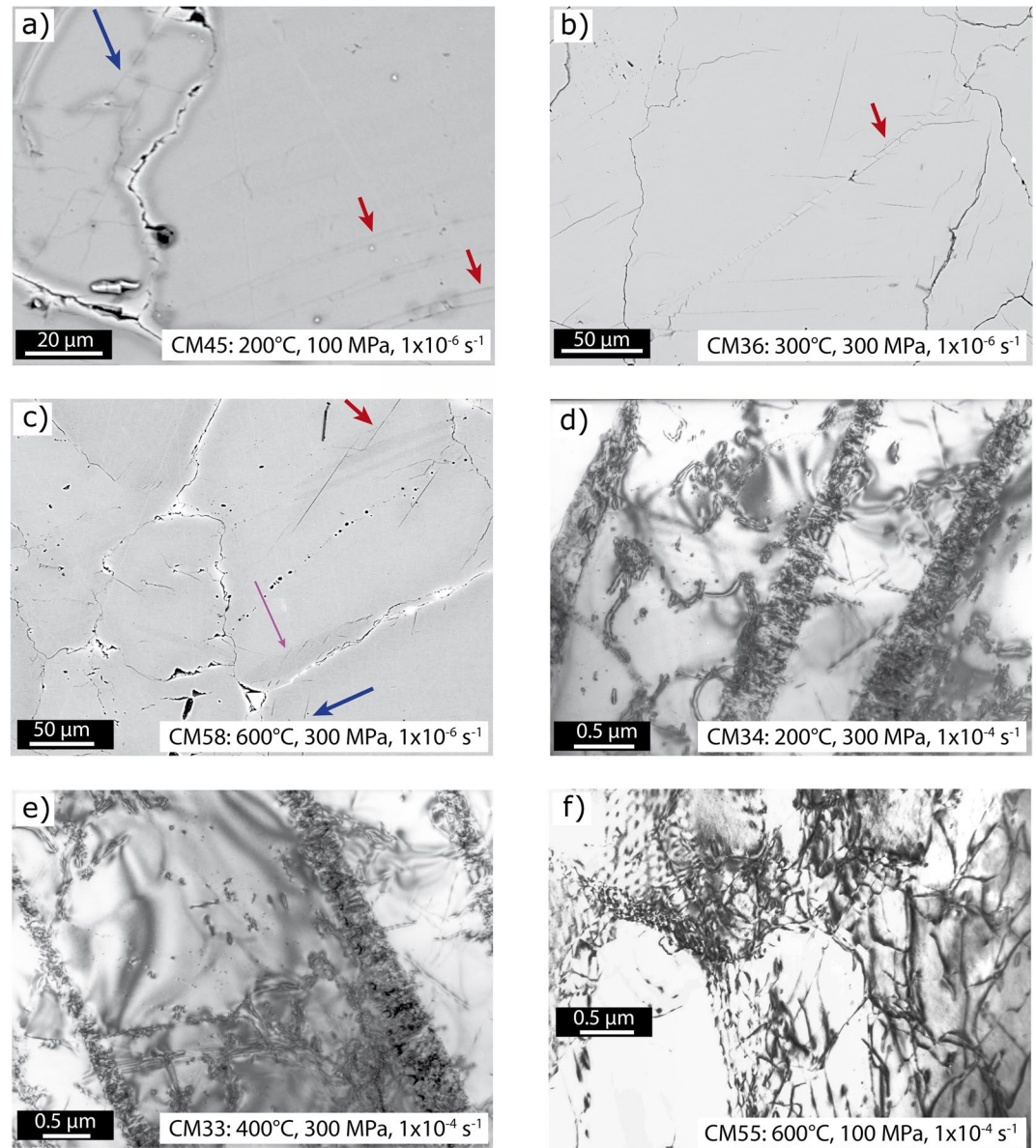


**Figure 9.** Back-scattered electron micrographs (BSED) (a–c) and transmission electron micrographs (TEM) of deformed samples taken with selected area diffraction conditions (d–f). (a) Parallel fractures probably lying along twin boundaries are marked by red arrows. A fracture network along a grain boundary has similar morphology as that shown in Figure 8d (marked by blue arrow). (b) The central feature (red arrow) shows cracks both parallel to twin boundaries and transecting the twin; together these form a granulated zone. (c) Crack swarms exist along grain boundaries (blue arrow), within large lobate twins (purple arrow), and in “stair-step” crack structures (red arrow) that intersect twins. The structures suggest that cracking and twinning are associated with each other even at higher temperatures. (d) Three twin boundaries run from upper right to lower left. Poorly organized tangles of dislocations occur along and between the boundaries. (e) Tangles of dislocations exist between the twins; interactions between the twin boundaries and dislocations on the interiors are evident. Dislocation densities vary both along the walls and perpendicular to them. (f) Dislocation microstructure formed at these temperatures show nascent organization into subgrain walls. Dislocations outside of the subgrain walls show interactions between and among the individual dislocations. The region around the scale bar is a hole caused by the argon thinning process used to make the sample. Samples and deformation conditions ( $T$ – $P_C$ – $\dot{\epsilon}$ ) are indicated.

**Table 2**  
Twin Densities of Selected Samples

Sample no	$P_C$ MPa	$\dot{\epsilon}$ s <sup>-1</sup>	$T$ °C	$\rho_{twin}$ tw/mm	$\Delta\rho_{twin}$ tw/mm	$\Delta\sigma_{0.1}$ MPa	$h_{0.1}$ MPa
CM22_1	300	1E-4	20	141	51	444	1,117
CM22_2				62	63		
CM34_1	300	1E-4	200	115	48	309	1,140
CM34_2				84	70		
CM25_1	300	1E-4	300	87	30	280	840
CM25_2				52	28		
CM25_3				102	40		
CM33_1	300	1E-4	400	128	51	262	558
CM33_2				101	64		
CM33_3				791	40		
CM65_1	300	1E-4	600	60	18	150	88
CM65_2				64	42		
CM65_3				83	36		
CM65_4				34	18		
CM69_1	300	1E-4	700	90	29	84	81
CM69_2				92	42		
CM69_3				58	21		
CM66_1	300	1E-4	800	72	32	47	52
CM66_2				84	71		
CM66_3				55	25		

## 4. Discussion

Many previous workers have documented brittle, semi-brittle, and crystal-plastic deformation in marbles over selected ranges of  $T$ ,  $P_C$ , and  $\dot{\epsilon}$  (e.g., Barnhoorn et al., 2004; Bruijn et al., 2011; Covey-Crump, 2001, 1998; Covey-Crump et al., 2016; de Bresser et al., 2005; Edmond & Paterson, 1972; Fischer & Paterson, 1989; Fredrich et al., 1989; Nardini et al., 2018; Nardini et al., 2020; Pieri, Burlini, et al., 2001; Quintanilla-Terminel & Evans, 2016; Rutter, 1974; Rybacki et al., 2013; Rybacki et al., 2014; Schmid et al., 1980; Scholz, 1968; Xu & Evans, 2010). This study provides data from 67 deformation tests having consistent protocols, thus allowing systematic comparison of microstructures and mechanical data. The results confirm that, under a surprisingly large range of conditions, that is,  $20 < T < 800^\circ\text{C}$ ,  $30 < P_C < 300$  MPa, and  $10^{-6} \leq \dot{\epsilon} \leq 10^{-3}$  s<sup>-1</sup>, Carrara marble deforms via semi-brittle flow up to  $\epsilon \leq 0.12$ . In this regime, almost all samples do not have macroscopic localized fracture zones and exhibit continuous hardening with coefficients that depend on pressure (Figure 3), temperature (Figure 5), and to some extent on strain rate (Figure 4). The only exceptions occur at two end conditions: First, brittle behavior accompanied by incipient strain localization and weakening occurs when  $P_C$  is less than about 50 MPa and  $T \lesssim 150^\circ\text{C}$ . Second, strength is no longer a function of  $P_C$ , when  $P_C \gtrsim 100$  MPa,  $T \gtrsim 600^\circ\text{C}$  and  $\dot{\epsilon} \leq 10^{-6}$  s<sup>-1</sup>.

In all the tests, observations of microstructures indicate that three deformation mechanisms operated concurrently: microcracking, twin formation, and dislocation motion. Presumably, these mechanisms jointly control strength and hardening. The relative contribution of each mechanism to the total inelastic strain depends on the applied temperature, pressure, and strain rate. In the Mbxx tests, where volumetric strain was measured, positive hardening coefficients were associated with slight compaction and an increase of axial  $P$ -wave velocity (Figures 6 and 7). The increase in velocity might owe to

closure of pre-existing grain boundary cracks. Following, we first briefly discuss the conditions for transition between regimes and the mechanisms prevailing in the different deformation regimes, followed by a comparison to twinning-induced plasticity in metals, a brief analysis of existing formal descriptions of semi-brittle creep, and possible implications for deformation for calcite rocks under geological conditions.

### 4.1. Comparing Results to Simple Estimates of the Brittle/Ductile and Brittle/Plastic Transitions

#### 4.1.1. The Brittle-Ductile Transition (BDT)

Early estimates of the pressure at BDT,  $P_{C\text{BDT}}$ , were based on equating the fracture strength of intact samples with the differential stress necessary to cause sliding along an optimally oriented, pre-existing fault (Byerlee, 1968). Assuming that frictional sliding is governed by rate-independent Mohr-Coulomb behavior and neglecting cohesive strength, the shear stress resolved onto the sliding plane is

$$\tau_{\text{slide}} = \mu \cdot \sigma_n \quad (3)$$

where  $\sigma_n$  is the normal stress resolved on the fault plane and  $\mu$  is the friction coefficient. Then, for an optimally oriented fault, frictional sliding under conventional triaxial loading occurs when the differential stress and  $P_C$  are related by

$$\Delta\sigma = r \cdot P_C \quad (4)$$

where

$$r = \left. \frac{\partial\Delta\sigma}{\partial P_C} \right|_{\epsilon=0.05} = \left[ (\mu^2 + 1)^{\frac{1}{2}} + \mu \right]^2 - 1 \quad (5)$$

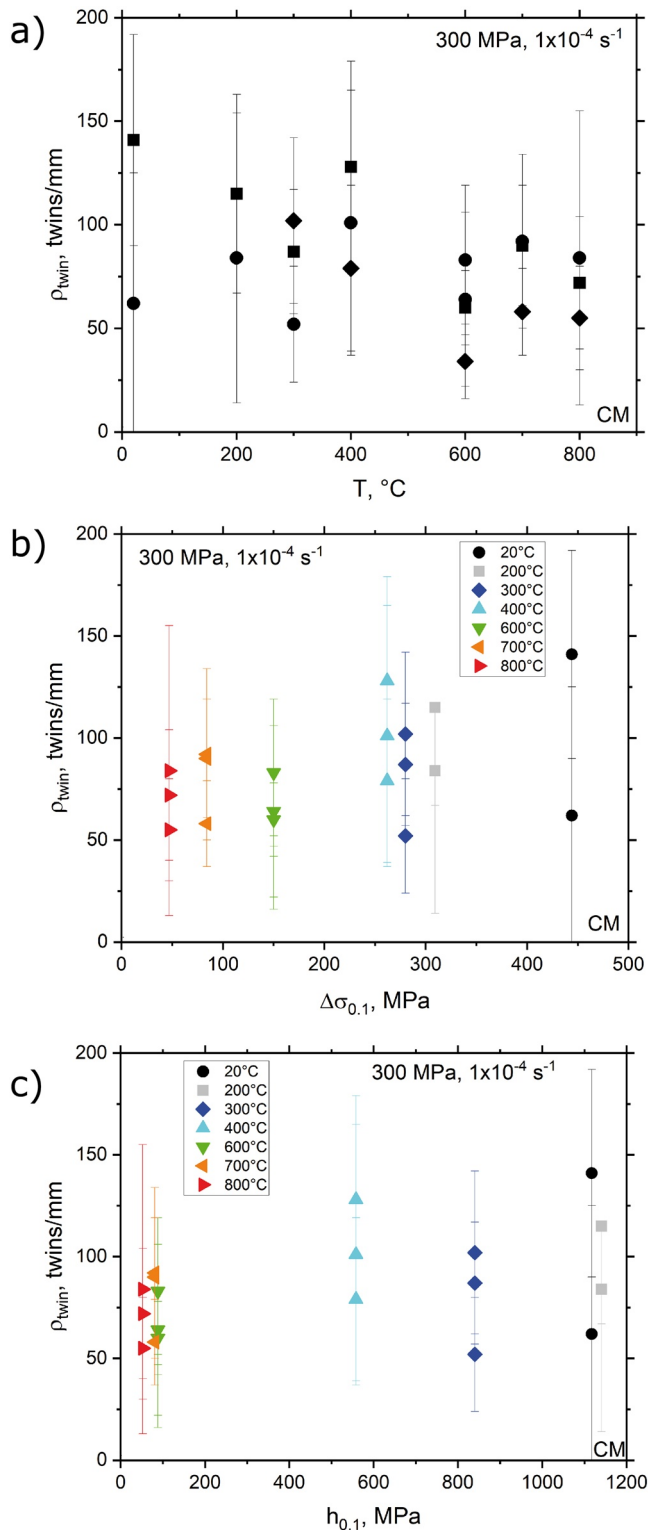


**Figure 10.** Twin density,  $\rho_{\text{twin}}$ , of samples deformed at  $P_C = 300$  MPa,  $\dot{\epsilon} = 1 \times 10^{-4} \text{ s}^{-1}$  and various temperatures. The density tends to increase with decreasing temperature (a), increasing strength,  $\Delta\sigma_{0,1}$  (b) and increasing hardening coefficient,  $h_{0,1}$  (c). The large scatter is attributed to limited area of measurement, uncertainty in twin discrimination, and user bias.

Zoback, 2007. If the friction coefficient of calcite gouge,  $\mu = 0.58$  (Carpenter et al., 2016), then  $\Delta\sigma \approx 2 P_C$ . Assuming instead  $\mu = 0.75$ , a proxy for clay-poor rocks (Sibson, 1983),  $\Delta\sigma \approx 4 P_C$ . In Figures 3a and 3c, we added thin dashed lines corresponding to  $r = 5, 2,$  and  $1$  ( $\mu = 1.02, 0.58$  and  $0.35$ , respectively). In our experiments, a thin, macroscopic, shear zone formed only at  $T = 20^\circ\text{C}$ ,  $P_{\text{C BDT}} < 50$  MPa, corresponding to  $r = 5$  ( $\mu \approx 1$ ). This value is quite similar to results given by von Kármán (Haimson, 2006; Ván & Vászárhelyi, 2010 and Fredrich et al., 1989). Edmond and Paterson (1972) measured larger  $P_{\text{C BDT}} = 50\text{--}100$  MPa at  $T = 20^\circ\text{C}$  and  $\dot{\epsilon} = 4 \times 10^{-4} \text{ s}^{-1}$ ; thus,  $r$  was lower, 2.8. Note that at higher  $T$ , we did not observe brittle behavior up to  $\epsilon < 0.12$ . The loading configuration is also important: The pressure for BDT in conventional triaxial extension is higher than in conventional triaxial compression (Heard, 1960). This effect can be reconciled by considering the axial stress as the least principal stress and the confining pressure as the greatest principal stress (Kirby, 1980). In this same vein, it may be that the ratio  $\Delta\sigma/\sigma_m$  (where  $\sigma_m$  is the mean stress) is determinative. In our experiments the BDT occurs when  $\Delta\sigma \approx 2\sigma_m$ , (or  $\Delta\sigma \approx 4 P_C$ , because, for conventional triaxial loading,  $\sigma_m = (\sigma_1 + 2\sigma_3)/3$ ).

It is clear that Byerlee's criterion is at best approximate, and certainly not rigorous, as recognized by Edmond and Paterson (1972). The transition from localized faulting to distributed fracturing implies that local microcracks propagate stably, rather than coalescing. Many factors might be important for fracture stabilization, including crack arrest at grain boundaries, twin boundaries, or other obstacles, changes in crack orientation during propagation, the development of large strain heterogeneities arising around finely distributed pores or included phases (Paterson & Wong, 2005; Wong & Baud, 2012), or blunting of the crack tips by dislocation flow. Of course, temperature, strain rate, and overall mineral composition are quite important (Heard, 1960; Kirby, 1980). For comparison,  $P_{\text{C BDT}}$  for various other rock types deformed in triaxial compression at  $T = 20^\circ\text{C}$  ranges from about 10 MPa for porous limestones, chalks, and rocksalt to 300–600 MPa for serpentinites, basalts, granites, and quartzites (Paterson & Wong, 2005).

It is also important to note, that, because dilatant damage in the form of microfractures is accumulating, weakening or even macroscopic failure might occur at strains higher than those of our experiments (Lyakhovskiy et al., 2015). Samples deformed at  $T = 20^\circ\text{C}$  and  $P_C < 50$  MPa exhibit pronounced dilatant behavior, velocity reductions, and weakening, and they also contain strongly crushed and granulated material along grain boundaries and within transgranular fractures (Figures 6 and 8a). Samples deformed at higher  $P_C$ , but the same strain rates and  $T$ , also show crushed boundary regions, but those regions do not extend over multiple grains (Figure 8b). It is plausible that continued damage production might lead to negligible hardening coefficients, or even weakening, at much higher strains. Brittle failure of Carrara marble has been reported at high strains in torsion experiments even when  $T = 500^\circ\text{C}$  and  $P_C = 300$  MPa (Barnhoorn et al., 2004). Such failure is probably initiated by cavitation (e.g., Verberne et al., 2017). However, it is worth remembering that strain weakening does not require fracturing. At  $T$  as high as  $727\text{--}927^\circ\text{C}$ , in torsion tests, the strength of Carrara evolves with strain (Pieri, Burlini, et al., 2001), hardening up to a shear strain of about one, followed by gradual weakening up to a shear strain of about 4, above which steady state is reached. Presumably at these elevated temperatures, the deformation mechanisms did not include fracturing.



Considering the behavior of rocks with preexisting faults as can be envisioned in the upper Earth's crust, it was shown by Meyer et al. (2019) that the BDT given by Byerlee's approach may represent an upper stress bound for localized deformation. The authors performed fault reactivation tests on Carrara marble at room temperature and  $P_c = 5\text{--}80$  MPa and measured an increasing partitioning of bulk strain and fault slip with increasing  $P_c$ , where bulk deformation occurred by semi-brittle processes. Due to strain hardening, partitioning starts at the pressure at which fault strength is larger than matrix yield strength and terminates at  $P_c$ , where fault strength is equal to matrix flow stress for which the fault is then locked. Both processes operate simultaneously in between the two end-member pressures and the partitioning is proportional to the ratio (fault strength–yield strength)/(matrix strength–yield strength). Accordingly, the transition from localized to distributed (ductile) deformation (LDT), may occur over a broad range of pressures (Meyer et al., 2019).

#### 4.1.2. The Brittle-Plastic Transition (BPT)

Once the sample is deforming in the semi-brittle regime, further increases in pressure (or mean stress) will suppress microfracturing, leading eventually to the dominance of crystal-plasticity, that is, the brittle-plastic transition, BPT. The increase in  $\Delta\sigma$  with increasing  $P_c$  becomes smaller and eventually  $\Delta\sigma \neq f(P_c)$ . The pressure at which this transition occurs can be used to define  $P_{c\text{BPT}}$ . Because of the systematics of crystal-plasticity,  $P_c$  will depend on  $T$  and  $\dot{\epsilon}$  (see Figures 4 and 5 and discussion by Kohlstedt et al., 1995). Goetze suggested a criterion for the BPT (as cited in Kohlstedt et al., 1995), based on the work of Edmond and Paterson (1972). In their study, the strength of Carrara marble deformed at  $T = 20^\circ\text{C}$  and  $\dot{\epsilon} = 4 \times 10^{-4} \text{ s}^{-1}$  was pressure independent when  $P_c \gtrsim 500$  MPa ( $\Delta\sigma \approx 475$  MPa), that is, when  $P_c \approx \Delta\sigma$  (Figure 3a). Thus, a general empirical observation motivating Goetze's criterion is that the pressure sensitivity of strength is suppressed when the work necessary to cause dilation is less than that necessary for non-dilatant shear. This observation is quite clearly an approximate estimate.

In fact, the Goetze criterion underestimates the onset of the BPT in our experiments. For example, at  $T = 600^\circ\text{C}$ ,  $\Delta\sigma \approx P_c$ , but strength is independent of  $P_c$  only when  $\dot{\epsilon} = 1 \times 10^{-6} \text{ s}^{-1}$  and at  $T = 800^\circ\text{C}$ ,  $\Delta\sigma$  is affected by  $P_c$  when  $\dot{\epsilon} = 1 \times 10^{-4} \text{ s}^{-1}$ , even though  $\Delta\sigma < P_c$  (Figure 2g and Table 1). In almost all the samples, we observed a few microcracks even at high temperatures (Figure 8). However, it is important to recognize that some microcracks, even those that are intragranular, could have formed during quenching and depressurization. The pressure dependence of strength at higher temperature in this study is quite consistent with earlier work by Fischer and Paterson (1989). Using a dilatometric technique, those authors measured volumetric strain at elevated temperatures for various effective pressure from 50 to 250 MPa. At  $T \geq 600^\circ\text{C}$  and  $\dot{\epsilon} = 1 \times 10^{-4} \text{ s}^{-1}$ , when the effective pressure is less than 150 MPa, there is slight dilation (vol. strain  $< 0.005$ ). Similar results are seen during deformation of other rock types. High-pressure, high-temperature deformation experiments done on basalt (Violay et al., 2012) and quartz gouge (Richter et al., 2018) suggest that the Goetze criterion predicts  $P_{c\text{BPT}}$  when  $T \approx 900^\circ\text{C}$  or higher than  $700^\circ\text{C}$ , respectively. In contrast, the BPT seems to be closer to  $\Delta\sigma \approx 2 P_c$  for quartz-rich rocks (Reber & Pec, 2018). Even at high  $T$ , if the imposed strain rate is too high, cavities may nucleate and lead to failure at high strains (e.g., Dimanov et al., 2007; Rybacki et al., 2010). Thus, as with Byerlee's estimate, although our lab data are in rough agreement with  $P_{c\text{BPT}} \approx \Delta\sigma$ , the criterion is completely empirical and is, at best, a rule of thumb.

A second estimate of the BPT, owing to Horii & Nemat-Nasser (H&NN) (1986), utilizes numerical and analytical solutions of the stress state around a dilating wing crack that extends from the end of a sliding microcrack. As pressure increases, strain accommodation shifts from dilational extension of the wing crack to crystal plastic flow around the end of the sliding crack. In their analyses, the mechanism that dominates is determined by two ratios: The first is ductility,  $D = K_{IC}/(\tau_y \sqrt{\pi c})$ , where  $K_{IC}$  is the critical stress intensity factor for mode I cracking,  $c$  is the half-length of the sliding crack, and  $\tau_y$  is the yield stress for dislocation flow. The second is the stress ratio,  $\sigma_3/\sigma_1$ . Large ductility or high relative confinement promotes crystal plasticity at the expense of microcracking. If the coefficient of friction along the sliding crack,  $\mu = 0.4$ , then crystal-plasticity dominates for all compressive confinements when  $D > 0.26$  and for all ductilities when the confinement ratio is greater than about 0.4 (Horii & Nemat-Nasser, 1986).

In our experiments, an upper limit to sliding crack length might be the grain size, thus,  $c \lesssim 100 \mu\text{m}$ . The fracture toughness  $K_{IC}$  for calcite at  $T = 20^\circ\text{C}$  is of the order of  $0.2\text{--}0.4 \text{ MPa}\cdot\text{m}^{0.5}$  (Atkinson, 1984; Atkinson & Avdis, 1980; Brace & Walsh, 1962; Broz et al., 2006; Gilman, 1960; Gupta & Santhanam, 1969). When  $\dot{\epsilon}$  is between  $1 \times 10^{-5}$  and  $1 \times 10^{-4} \text{ s}^{-1}$ ,  $\tau_y$  for  $r$  slip is about 197 MPa at  $20^\circ\text{C}$  and  $\approx 41$  MPa at  $200^\circ\text{C}$ . The critical resolved shear stress (CRSS) for  $f$  slip is slightly greater, about 206 MPa at  $20^\circ\text{C}$  and 74 MPa at  $200^\circ\text{C}$  (de Bresser

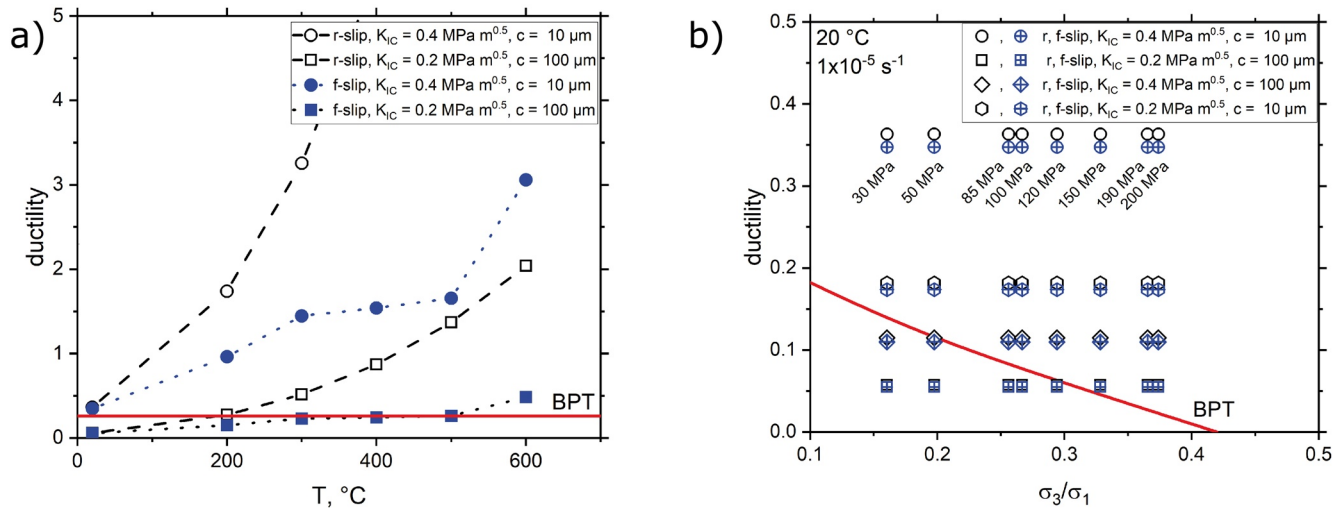


**Figure 11.** Ductility (defined by Horii and Nemat-Nasser, 1986; see text) vs. temperature (a) and stress ratio (b). Estimates are based on the critical resolved shear stress for  $r$  and  $f$  slip in calcite. For each system, we assume either low fracture toughness ( $K_{IC} = 0.2 \text{ MPa m}^{0.5}$ ) and large initial crack length of  $\approx$  half the grain size ( $c = 100 \mu\text{m}$ ) or high fracture toughness ( $0.4 \text{ MPa m}^{0.5}$ ) and  $c = 10 \mu\text{m}$  to explore possible limits. (a) The critical ductility at which crystal-plasticity dominates for all stress ratios is 0.26 (indicated by solid line). When  $T \geq 200^\circ\text{C}$ , the conditions for the BPT are met for all assumed values. (b) Ductility vs. stress ratio for experiments conducted at  $T = 20^\circ\text{C}$ ,  $\dot{\epsilon} = 1 \times 10^{-5} \text{ s}^{-1}$ . Ductility is calculated for  $r$  and  $f$  slip and all combinations of  $K_{IC}$  and (c) Labeled pressures represent  $P_C$  values. The BPT is predicted to occur when the experimental parameters fall in the upper-right hand portion of the graph, that is, above the solid line. The only experiments likely to remain in the brittle regime are those conducted at pressures below  $\approx 150 \text{ MPa}$ . However, in most experiments (except at  $P_C$  of 30 and 50 MPa) strength was pressure dependent; thus, the BPT, as defined here, was not achieved.

& Spiers, 1997). Using these values and estimating the bounds for  $K_{IC} = 0.2 \text{ MPa m}^{0.5}$ ,  $c = 100 \mu\text{m}$  and  $K_{IC} = 0.4 \text{ MPa m}^{0.5}$ ,  $c = 10 \mu\text{m}$ , the ductility for  $r$  slip at  $T = 20^\circ\text{C}$  is between 0.36 and 0.06, respectively. At  $T = 200^\circ\text{C}$ ,  $r$ -slip ductility lies between 0.28 and 1.74, that is, near to or well above the critical value of  $D = 0.26$  (solid line in Figure 11a). For  $f$  slip,  $D$  values are comparable at room temperature and about 50% less than for  $f$  slip at  $T = 200^\circ\text{C}$ . For all the experiments at  $T \geq 200^\circ\text{C}$ , the analysis of  $H\&NN$  predicts that the BPT has been reached, except for the most restrictive interpretations of the fracture toughness and initial crack size, that is, for  $f$  slip with minimum  $K_{IC}$  and longest crack length.

In our experiments, the stress ratios at room temperature are typically above 0.30 at  $P_C \geq 150 \text{ MPa}$ . Plots of the ductility vs. stress ratios for the various tests at  $T = 20^\circ\text{C}$  are shown in Figure 11b. Ductility and stress ratios are sufficient for the BPT (solid line in Figure 11b), except when pressures are less than  $\approx 150 \text{ MPa}$ . Thus, because the strength is still pressure dependent at higher  $P_C$  and  $T = 20$  and  $200^\circ\text{C}$ , the  $H\&NN$  criteria fail to predict the BPT. The criteria do coincide with the disappearance of weakening as pressure is increased above  $\approx 150 \text{ MPa}$  (i.e., are close to the BDT).

$H\&NN$ 's treatment has the advantage that a specific micromechanical model is prescribed, but the model has some limiting simplifications. Although the critical values of the two ratios are specified for dominance of crystal plasticity,  $H\&NN$  note that, in most circumstances, the initial deformation includes a brief period during which brittle crack extension precedes crystal-plastic yielding. Thus, inelastic yielding might have some slight pressure dependence even when the deformation is dominated by crystal-plasticity. Their analyses do not include rate-dependence of either mechanism, nor do they include the effect of strain hardening. In addition, both fracture toughness and critical resolved shear stress for slip in calcite is quite anisotropic. Thus, it is not clear whether the correct yield stress to be used should be that of the easiest slip system, the harder slip system, or some combination thereof. In summary, all three estimates, Byerlee's treatment, the Goetze criterion, and  $H\&NN$ 's analyses, are approximate predictors of  $P_{C \text{ BDT}}$  and  $P_{C \text{ BPT}}$  in laboratory experiments; all are deficient in some regard, and all have both practical and theoretical limitations.

## 4.2. Twinning Induced Plasticity in Calcite

### 4.2.1. Interactions Among Twinning, Dislocation Glide, and Cataclasis in Calcite Rocks

There is abundant evidence from earlier studies and from this work that cataclasis, dislocation flow, and twinning are inextricably related to each other during deformation at  $T \lesssim 600^\circ\text{C}$ . From the observed complex deformation behavior and resulting microstructures we infer that the relative contribution of each mechanism to the total inelastic strain depends on the applied temperature, pressure, stress, and strain rate. The influence of stress on twin structure is striking and twin frequency has frequently been used as an empirical constraint on paleostress (Jamison & Spang, 1976; Lacombe, 2007; Lacombe & Laurent, 1992; Laurent et al., 2000; Parlangeau et al., 2019; Parlangeau, Lacombe, Schueller, et al., 2018; Rowe & Rutter, 1990; Rybacki et al., 2011, 2013). Temperature is also important (Burkhard, 1993). In our experiments, the number of twins decreases as  $T$  increases and the sample strength at the end of the test decreases. In addition, the twin thickness markedly increases. By analyzing naturally deformed limestones, Ferrill et al. (2004) correlated twin thickness and shape with the temperature of deformation, finding thicker, more lobate twins as  $T$  increased. The twin morphologies found in our experiments are roughly consistent with these trends.

The mechanical behavior and microstructures in our experiments show that two sets of conditions are end members: Strengths are strongly pressure-sensitive at low  $T$  ( $<200$ – $300^\circ\text{C}$ ), indicating dilatant behavior. For the other set of end-member conditions,  $T \gtrsim 600^\circ\text{C}$ ,  $P_c \gtrsim 50$  MPa, and low  $\dot{\epsilon}$ , pressure sensitivity of strength is low (although still existent) and mechanical behavior is dominated by crystal-plastic behavior. In the intermediate range of  $P_c$  and  $T$ , twinning, dislocation creep, and dilatant microcracking jointly control strength and hardening of the samples. Strikingly, both  $\Delta\sigma_{0.05}$  and  $h_{0.05}$  are relatively insensitive to temperature in the range between  $\approx 200$ – $400^\circ\text{C}$ , but strongly decrease with increasing  $T$  above  $\approx 400^\circ\text{C}$ . The latter is probably associated with the activation of  $f$  slip (high  $T$ ) and basal slip, whereas at  $T \approx 200$ – $400^\circ\text{C}$  the CRSS for  $e$ -twinning,  $r$  and  $f$  slip (low  $T$ ) does not change considerably with temperature (Barber et al., 2007; de Bresser & Spiers, 1997). Below about  $T = 200^\circ\text{C}$  the CRSS for  $r$  and  $f$  slip (low  $T$ ) strongly increase, consistent with the moderate increase of strength found at higher  $P_c = 300$  MPa when  $T$  is decreased from  $200^\circ\text{C}$  to  $20^\circ\text{C}$  (Figure 5). When  $P_c \leq 100$  MPa and  $T = 20^\circ\text{C}$ , hardening coefficients,  $h_{0.05}$ , are reduced, suggesting that the weakening effect of cataclasis outweighs the strengthening resulting from the temperature sensitivity of crystal plastic processes. Increased cataclasis is also suggested by the  $P$ -wave velocity reduction at low  $P_c$  (Figures 6 and 7).

The intense interactions among the three mechanisms are particularly evident from the examination of the microstructures, which strongly suggest that the three deformation mechanisms operate concurrently (e.g., Figures 8 and 9). Cracks are often contained within the twins, either parallel to the boundaries or at high angles to them. These microfractures often combine to form lacey patterns along the twins, likely indicating that the cracks post-date the twins. In other cases, twins terminate along internal microfractures, suggesting the converse, that is, fractures predate the twins. Intersecting twins often are the sites of Rose channels or short cleavage fractures between the two twins (Barber & Wenk, 1979). Dislocations interact vigorously with twins which likely form barriers restricting slip (for example, see Barber & Wenk, 1979; Fredrich et al., 1989). TEM micrographs (Figures 9d and 9e) also often show strong variations in dislocation density both along the strike of twin boundaries and perpendicular to them. These variations in density might be responsible for stress concentrations that could induce microcracking.

Twinning is also affected by the other two mechanisms. Twin deformation in calcite is notable because the stress to initiate twins in single crystals is very low, 4–10 MPa, (de Bresser & Spiers, 1993, 1997; Parlangeau et al., 2019). However, in polycrystalline rocks, the stress necessary to cause a twin to be initiated and remain (i.e., permanent twinning) is greater (65 MPa at  $200^\circ\text{C}$ ) and is affected by the grain structure (Covey-Crump et al., 2017). In those experiments, uniaxial deformation of Carrara marble and Solnhofen limestone was observed in situ using neutron diffraction. Elastic twins were produced under stresses of 15 MPa. The larger stresses needed for permanent twinning might result from the need to accommodate strain heterogeneities at the termination of a twin when it intersects a grain boundary (Covey-Crump et al., 2017; Kaga & Gilman, 1969; see also Figure 9 in Quintanilla-Terminel & Evans, 2016). At very high pressures and large strains, there can also be interactions between twin boundaries and deformation lamellae that alter the twin morphology in profound ways (Schuster et al., 2019).

Several of the twin piezometers alluded to above have the form:

$$\Delta\sigma = \sigma_{\text{twsp}}^o + k_{\text{twsp}}d_{\text{twsp}}^{-1/2} \quad (6)$$

where  $d_{\text{twsp}}$  is the twin spacing, and  $\sigma_{\text{twsp}}^o$  and  $k_{\text{twsp}}$  are constants (Rybacki et al., 2013). There is considerable scatter in data used to derive these relationships, arising in part from the difficulty in measuring twin densities using optical techniques, especially when the spacings are small. In addition, twin spacing is also sensitive to other parameters, including temperature, grain size, and crystallographic fabric (Covey-Crump et al., 2017; Ferrill, 1998; Rowe & Rutter, 1990). Twin volume and morphology are also important, but we were unable to measure these parameters with accuracy. It is likely that measurements using EBSD techniques would be more precise (Parlangeau, Lacombe, Lucas, et al., 2018). Despite the uncertainty in the twin piezometer, it is useful to notice that it is of similar form to an empirical relation of dislocation density and stress:

$$\Delta\sigma = \Sigma_{\text{dis}}^o + k_{\text{dis}}\rho^{1/2} \quad (7)$$

where  $\Sigma_{\text{dis}}^o$  and  $k_{\text{dis}}$  are constants, and  $\rho$  is the dislocation density (de Bresser, 1996). Then combining Equations 5 and 6, gives an empirical relation between dislocation density and twin spacing:

$$\left[ \frac{(\Sigma_{\text{dis}}^o - \sigma_{\text{twsp}}^o)}{k_{\text{twsp}}} + \frac{k_{\text{dis}}}{k_{\text{twsp}}}\rho^{1/2} \right]^2 = d_{\text{twinsp}}^{-1} \quad (8)$$

If the stress,  $\Delta\sigma$ , varies independently with  $\rho$  and  $d_{\text{twsp}}$  then the yield strength when  $\rho$  is very small or  $d_{\text{twsp}}$  is large,  $\sigma_{\text{yield}}^o$  should equal  $\Sigma_{\text{dis}}^o$  and  $\sigma_{\text{twsp}}^o$ . Under these assumptions, dislocation density and twin spacing would be inversely related,

$$\left( \frac{k_{\text{dis}}}{k_{\text{twsp}}} \right) \rho \approx d_{\text{twinsp}}^{-1} \quad (9)$$

This empirical relation is roughly consistent with experimental results for marbles, but it contains the critical assumption that dislocation density and twin density are independently related to stress. Given the microstructural observations presented above, this independence seems unlikely. As discussed below, it seems more likely that the effect of twin spacing on the mean free path for dislocation glide is responsible for hardening.

#### 4.2.2. Analogy of Calcite Deformation to TWIP in Metals

Dense, coarse-grained, calcite rocks exhibit several characteristic mechanical behaviors during triaxial compression experiments: Twinning, dislocation flow, and cataclastic deformation coexist even at low temperatures. Twin production requires low critical resolved shear stress, and hence, twin boundary energies must be small. Also, hardening coefficients during semi-brittle flow are very large. For example, in our experiments at  $T \leq 400^\circ\text{C}$ , hardening coefficients were often above 1 GPa, that is, about 3% of the shear modulus,  $\approx 30\text{--}34$  GPa (Carmichael, 1989). Similar behavior occurs in manganese-rich steels and some hexagonal metals and is called twinning induced plasticity (TWIP). In these metals, high hardening coefficients, owing to twinning, are responsible for extended service under severe loading conditions.

There are two relationships between twinning and dislocation glide that seem to be necessary for TWIP behavior (for an extensive review see De Cooman et al., 2018). First, twinning must be a low-energy process compared to dislocation glide. Thus, in these metals, the inception of dislocation flow and twinning are nearly concurrent during initial yielding. Secondly, the dominant glide planes must be oriented at high angles to the twin planes. Then, because twin boundaries are commonly opaque to crossing dislocations, twin formation reduces the mean-free path of dislocation glide. Twinning and slip in calcite obey all these criteria. The resolved shear stress necessary for twinning is the same as or lower than that necessary for  $r$  slip (Covey-Crump et al., 2017; de Bresser & Spiers, 1993, 1997; Parlangeau et al., 2019; Paterson, 1985). Another similarity between calcite and TWIP metals is that the temperature range over which hardening occurs is less than half the melting point. At these conditions, diffusive recovery processes are restricted, which promotes hardening. Based on these analogies, we contend that TWIP behavior is quite likely in our experiments and that twinning is a large contributor to both strain hardening and ductility of calcite rocks at low to moderate temperatures.

The empirical relation between twin spacing and stress (Equation 6) is very similar to the Hall-Petch relation relating grain size and yield strength (Cordero et al., 2016; Yu et al., 2018). As hardening occurs, twin spacing

decreases, and so, the term “dynamic-Hall-Petch effect” is often used to describe the change in strength with ongoing deformation (Bouaziz et al., 2008; De Cooman et al., 2018). The exact cause of this relation is still a subject of discussion, but a foundation assumption in all the models is that dislocation glide dominates deformation. In general, hardening caused by twin production is treated by considering one or more of the following: (a) isotropic models that include a decrease in dislocation mean free path owing to the opacity of the twin boundaries, (b) kinematic models that include back stresses owing to dislocation pile-ups at the twin boundaries, or (c) kinematic models that consider plastic strain incompatibilities between the twins and the matrix (Ashby, 1970; Bouaziz, 2012; Bouaziz et al., 2008; Cordero et al., 2016; De Cooman et al., 2018; Yu et al., 2018). Details, including the number of internal variables and the exact mechanism of the interactions between dislocation and twins, vary for each model.

For illustration, consider an isotropic Hall-Petch model for hardening that uses one internal dislocation variable (Bouaziz et al., 2008; Bouaziz & Guelton, 2001). The shear strength of the polycrystal ( $\tau$ ) is related to the square root of the total dislocation density,  $\rho_d$ , by a Taylor relation, similar to Equation 6:

$$\tau = \tau_0 + \alpha b \mu_s \sqrt{\rho_d} \quad (10)$$

where  $\alpha$  is a constant,  $b$  the Burgers vector, and  $\mu_s$  the shear modulus. The change in dislocation density during work hardening is given using the Kocks and Mecking (2003) relation, which describes the evolution of dislocation density as a function of the mean free path  $\lambda$ . The inverse of the mean free path,  $1/\lambda$ , is given by sum of the inverse of the characteristic spacings of obstacles to glide. These include dislocation spacing,  $1/(k\sqrt{\rho_d})$ , where  $k$  is a constant; twin spacing,  $d_{\text{twsp}}(\epsilon)$ ; and grain size,  $d$ . Finally, the Kocks-Mecking equation allows for decreases in dislocation density owing to dynamic recovery by subtracting a term given by a recovery factor,  $f$ , times  $\rho_d$ :

$$\frac{d\rho_d}{d\epsilon} = \frac{1}{b\lambda} - f\rho_d = \frac{1}{b} \left( \frac{1}{d} + \frac{1}{d_{\text{twsp}}} + k\sqrt{\rho_d} \right) - f\rho_d. \quad (11)$$

According to this simplified model, hardening increases with decreasing twin spacing, increasing dislocation density, and reduced recovery rate. More complex isotropic models distinguish between forest and mobile dislocations or incorporate a description for strain rate controlled by thermally activated passing of dislocations through obstacles. All these models have a common feature that the mean free path is affected by  $d_{\text{twsp}}$ , dislocation structure, and grain size. The two other classes of kinematic models consider the effect of internal stresses caused either by dislocation pile-ups (Bouaziz et al., 2008; Estrin & Kubin, 1986) or by accommodation stresses caused by strain discontinuities at the twin/matrix boundaries (Brown & Clarke, 1975; Gil Sevillano & de las Cuevas, 2012). Using full-field elasto-viscoplastic calculations, Arul Kumar et al. (2016) and Arul Kumar et al. (2015) showed that strain accommodation at twin terminations results in large inhomogeneous stress concentrations along the twin-matrix interface and that there are substantial differences in average shear stress in the twin and matrix. These calculations emphasize the importance of back stresses developed at twin/grain boundary intersections on twin growth.

#### 4.2.3. Changes in Strain Partitioning With Changes in $P_c$ , $T$ , and $\dot{\epsilon}$

In addition to the complex interplay of twinning and dislocation creep, as is found in TWIP metals, marbles also have substantial contributions to inelastic strain owing to microfracturing. The observed microstructures suggest that strain inhomogeneities that develop at twin terminations can be relieved by either dilatant microcracking at low pressures and temperatures or by dislocation processes (see our Figure 9 and Quintanilla-Terminel & Evans, 2016; Spiers, 1981). In addition, microfractures are often contained within the twin structures, either lying along the boundaries or located internally.

The strain to failure (often called ductility in engineering publications) is greatly increased in TWIP metals (De Cooman et al., 2018). During semi-brittle deformation of marble, twinning requires relatively low resolved shear stresses. Thus, in properly oriented grains, it is an early contributor to the inelastic strain of the aggregate. However, because these grains become harder as they twin, further inelastic strain is transferred to grains with lower twin densities. By analogy to the TWIP materials, the strain delocalization resulting from strain transfers from one grain to another may be a major reason for the prolonged period of semi-brittle behavior observed over a wide range of conditions in calcite.



Strain partitioning amongst the three processes is affected by strain rate, temperature, and pressure. For TWIP metals, where microfracturing is much less prevalent than in the marbles, changing temperature and strain rate seems to alter the rate of dislocation accumulation during hardening (Ardeljan et al., 2016). The dislocation creep mechanisms themselves may change as deformation conditions vary. At lower temperatures, the stress necessary to cause dislocation motion tends to become less sensitive to changes in strain rate and  $T$  owing to inhibition of cross-slip and climb at lower temperatures. Similarly, in calcite rocks a transition from rate-sensitive to rate-insensitive flow occurs at about  $T = 400^\circ\text{C}$  (e.g., Covey-Crump, 1998, 1994; Renner & Evans, 2002; Renner et al., 2002; Rutter, 1974). As seen in Figures 4 and 5, both the stress and hardening coefficients at  $\epsilon = 0.05$  in our experiments are much less sensitive to changes in rate and temperature in the range  $200 < T < 400^\circ\text{C}$ , than at higher  $T$ .

In the Carrara experiments, the effect of pressure on stress and hardening coefficient can be viewed as indicating the intensity and effect of microfracturing at given conditions. At  $T = 20^\circ\text{C}$ , both stress and hardening coefficient uniformly increase with increasing pressure at all strain rates (Figures 2a and 2b), probably indicating that dilatant microfracturing is being suppressed. However, for fixed pressures, stress is much less responsive to changes in strain rate than is the hardening coefficient. At  $T = 20^\circ\text{C}$  and  $100 < P_c < 300$  MPa,  $h$  decreases with increasing strain rate, whereas  $\Delta\sigma$  increases (Figures 2a, 2b and 4a, 4c). If we view increasing  $h$  as indicating enhanced twin activity and increased dislocation storage, then it is plausible that increasing the rate of deformation might increase the rate of one or both. On the other end of the temperature spectrum, at  $T = 600^\circ\text{C}$  (Figures 2g, 2h and 4a–4c), the effect of changing strain rate is larger than that of changing pressure, as might be expected if crystal plasticity dominated inelastic strain. It is surprising to notice that at these elevated temperatures, some dilatant processes are still occurring at the faster strain rates. In the temperature interval between 200 and  $400^\circ\text{C}$ , the effects of changes in  $P_c$  are reduced from that occurring at lower  $T$ , and the effects of  $\dot{\epsilon}$  are much less distinct. It is plausible that microfracturing, hardening, and dislocation creep respond to the changing conditions and compete to accommodate strain.

Changes in the partitioning of inelastic strain amongst the three mechanisms can be expected to influence twin morphology as well. Because twin growth (i.e., widening) requires climb of defects along the twin boundary and because back stresses caused by strain accommodation at the twin termination will be reduced, one expects thicker twins at higher  $T$  and lower  $\dot{\epsilon}$  (Arul Kumar et al., 2015, 2016), as has been observed by Ferrill et al., (2004) in calcite rocks. At yet higher temperatures, local strain heterogeneities could also be relieved by both dynamic and diffusive recovery.

Although the extensive work on TWIP metals yields insights that can be applied to the deformation of marble, many questions remain. For example, how exactly (in a quantitative way) do the three mechanisms change in partitioning over larger changes in the conditions of  $T$ ,  $P_c$ , and  $\dot{\epsilon}$ ? This question is critical in extrapolating the experimental results to natural conditions in the Earth. Secondly, how does the twin volume fraction change during straining, and how does the twin fraction relate to the overall stress? Many studies of TWIP in metals suggest that twin volume might saturate at larger strains. There is some suggestion that saturation might occur in Carrara (Rybacki et al., 2013), but only measurements of twin spacing—as opposed to twin volume—are available so far. Even those measurements contain a great deal of scatter. Third, can the knowledge of strain partitioning amongst the three mechanisms be used to constrain the loading conditions in naturally deformed rocks?

### 4.3. Constitutive Laws for Semi-Brittle Deformation

Owing to the complexity and interaction of the mechanical processes occurring under semi-brittle behavior, it is not surprising that no single constitutive equation exists that includes all the microphysical processes that may be involved. One particular difficulty is determining the correct way to describe the combined operation of brittle and plastic processes. For example, the processes might be parallel-concurrent or series-sequential, yielding upper and lower strength estimates (Ding et al., 2021).

Early attempts at semi-brittle creep laws were empirical rather than mechanistic. For example, shear strength  $\tau$  might be estimated by

$$\tau = \phi\tau_{\text{plas}} + (1 - \phi)\tau_{\text{MC}} \quad (12)$$



where  $\tau_{\text{plas}}$  is plastic shear strength,  $\tau_{\text{MC}}$  is Mohr-Coulomb (cataclastic) failure strength and  $\phi = \tanh(c_1 \cdot \sigma_n)$  and  $c_1$  is a material constant (Chester, 1988; Ding et al., 2021). An alternate description (Okazaki et al., 2021; Shimamoto & Noda, 2014) is

$$\tau = \tau_{\text{plas}} \cdot \tanh\left(\frac{\tau_{\text{fric}}}{\tau_{\text{plas}}}\right) \quad (13)$$

where  $\tau_{\text{fric}}$  is frictional strength. In both cases, brittle and plastic strength are combined assuming a simple trigonometrical relationship. Other empirical models involve a volume-weighted sum of plastic and brittle strength (Beall et al., 2019; Handy et al., 1999). Bos and Spiers (2002) and Niemeijer and Spiers (2007) suggested a description of phyllosilicate-rich fault rocks, where the plastic deformation is assumed to be governed by pressure solution. Coupled plastic-damage continuum-mechanics models were suggested to describe the semi-brittle mechanical behavior of shales (Guéry et al., 2008; Parisio & Laloui, 2017; Parisio et al., 2015). In addition, a number of combined rheological models were formulated for the description of transient creep of rocks (e.g., Hou et al., 2019; Kamali-Asl et al., 2018; Yang & Li, 2018). On a larger scale, localization and shear zone development across the BDT was analyzed using analytical and numerical modeling approaches (e.g., Jammes et al., 2015; Lavier et al., 2013).

Several treatments have focused on microphysical descriptions of the brittle processes. For example, semi-brittle flow might be governed by time-dependent cataclasis owing to sub-critical crack growth. Such stress corrosion may be induced by hydrolysis of bonds if water is present. Although dislocation creep in Carrara marble is hardly affected by water at low temperatures (de Bresser et al., 2005; Rutter, 1974), sub-critical crack propagation does occur when fluids are present (Brantut et al., 2014; Henry et al., 1977; Rostom et al., 2013; Røyne et al., 2011). Other processes including microplasticity, ion exchange and atomic diffusion might also induce brittle creep (Brantut et al., 2013). To account for stress corrosion, Brantut et al. (2012) extended Ashby and Hallam's (1986) wing crack model to include sub-critical crack growth by applying Charles's (1958) law. This model can simulate primary, secondary and tertiary creep phases commonly observed during constant stress tests. For the minimum (secondary) creep rate, the effect of confining pressure and temperature can be considered. This microphysical approach may be used to describe semi-brittle deformation of wet rocks at low temperature. However, at higher temperatures, crystal-plastic processes certainly play a role, and the contributions of these mechanisms to the total strain (rate) will need to be included.

Transient dislocation creep is a second important aspect of semi-brittle behavior. Covey-Crump (1994, 1998, 2001) was the first to formulate a phenomenological description of the creep deformation of marble using a single empirical internal state variable, as suggested by Hart (1970, 1976). This approach can describe aspects of the transient and relaxation behavior of Carrara marble at fixed pressure, but it cannot explicitly account for the influence of changes of  $P_C$  on strength because brittle damage is excluded. More recently, visco-plastic self-consistent (VPSC) models using microphysical descriptions of dislocation slip have been applied to determine deformation in a polycrystal (Lebensohn & Tome, 1993; Morales et al., 2014; Tommasi et al., 2000; Wallis et al., 2019; Xu & Evans, 2010). By calculating a self-consistent mechanical state in each grain for each deformation step, the development of a crystallographic preferred orientation can be monitored. VPSC modeling is a promising method to account for hardening by both dislocation slip and twinning (e.g., Beyerlein & Tome, 2008; Brown et al., 2012; Segurado et al., 2018; Wang et al., 2010). However, as with Hart's method, the analysis is restricted to crystal-plastic deformation; brittle processes have not been included thus far.

In a more recent attempt to describe the brittle and semi-brittle deformation of carbonates, Nicolas et al. (2017) developed a model based on three microphysical mechanisms: (a) brittle propagation of wing cracks generated by sliding along pre-existing fractures; (b) plastic deformation of pre-existing voids, including hardening induced by increasing forest dislocation density; and (c) nucleation of new cracks owing to dislocation pile-ups. This treatment is a significant advance because it considers the concurrent operation of both crystal-plastic and cataclastic mechanisms. Thus, the relative contributions of each microphysical mechanisms to total strain can be assessed. The treatment is isotropic, that is, individual grain orientation is not considered, and it is assumed that the mechanisms do not interact with each other. The model was applied to deformation data from porous limestones in the brittle and semi-brittle regime, and successfully produced plausible descriptions of the transition from shear-enhanced compaction to overall dilation.

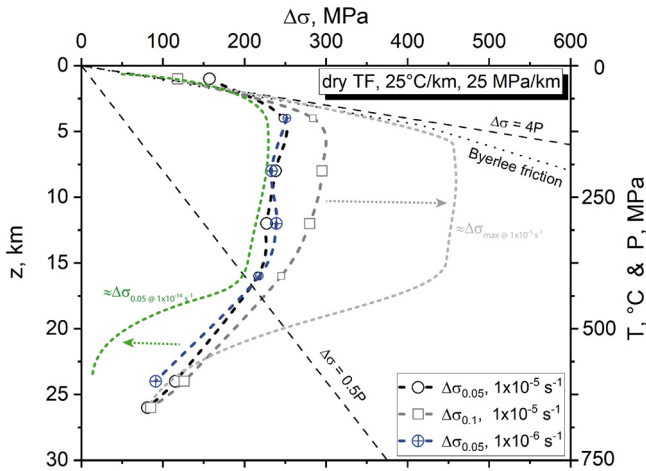


**Figure 12.** Hypothetical differential stress-depth plot for deformation of dry Carrara marble, constructed for a simplified temperature and pressure gradient of  $25^{\circ}\text{C}/\text{km}$  and  $25\text{ MPa}/\text{km}$ , respectively. Stress at 0.05 strain and a laboratory strain rate of  $\dot{\epsilon} = 1 \times 10^{-5}\text{ s}^{-1}$  (open circles) is estimated to be relatively constant at middle crust depth level, where semi-brittle deformation prevails. Due to hardening in this regime, differential stress increases with strain (measured at  $\epsilon = 0.1$ , open squares) and may reach maximum strengths ( $\Delta\sigma_{\text{max}}$ ) as deduced from high strain torsion tests. The low sensitivity of stress (at 0.05 strain) to strain rate in the semi-brittle domain is shown for  $\dot{\epsilon} = 1 \times 10^{-6}\text{ s}^{-1}$  and speculated for  $\dot{\epsilon} = 1 \times 10^{-14}\text{ s}^{-1}$  (green line), where low strain rate mainly affects strength at high temperature with dominantly plastic deformation. Byerlee's friction law for thrust faults (TF) and stress-pressure gradients of  $\Delta\sigma = 4 P_C$  and  $\Delta\sigma = 0.5 P_C$  are shown for comparison, where the latter may roughly coincide with the BDT and BPT, respectively. Large symbols show measured data, small symbols interpolated data (see text for details).

Despite the very positive aspects of this treatment, there are some complexities that are missing. In particular, the effects of twinning, dynamic recovery, and the transition from distributed cataclasis to localized flow are not included. Nor did the model consider cracking induced by twinning or sub-critical crack growth. In the Nicolas et al. model, the hardening coefficient is supposed to be related to the current density of forest and mobile dislocations, and to the grain size, but twin spacing is not considered (cf. Equation 11). In TWIP metals, twinning increases hardening coefficients over those due to dislocation storage by a substantial amount. In addition, from the observation of microstructures, we suppose that cracking associated with twinning might also be a strong contributor to damage production. It is beyond the scope of this paper to present an advanced model that includes these additional complexities, that is, cracking and comminution, cataclasis, twinning and dislocation activity and their mutual interactions over the entire range of  $P_C$ - $T$ - $\dot{\epsilon}$  conditions observed here. A more detailed analysis of the partitioning of these different mechanisms is required to identify the prevailing state variables that control the deformation and needs to be addressed in subsequent work.

#### 4.4. Geologic Applications

Although semi-brittle deformation may prevail over a large range of depths in the Earth, particularly for polyphase rocks, this regime is poorly constrained so far due to its complexity. A simple strength profile estimation for dry Carrara marble is shown in Figure 12 assuming a linear temperature and pressure gradient with depth of  $25^{\circ}\text{C}/\text{km}$  and  $25\text{ MPa}/\text{km}$ , respectively. Note that we use the stress data as measured at lab strain rates, and then perform an extrapolation to slower rates, without the benefit of a rigorous constitutive law. Brittle behavior is likely limited to crustal depths of a few kilometers and brittle strengths are often assumed to be bounded by friction following Byerlee's law (dotted line in Figure 12). Our stress data measured at  $\dot{\epsilon} = 1 \times 10^{-5}\text{ s}^{-1}$

and  $\epsilon = 0.05$  strain (open circles) indicate a strong increase with pressure, equivalent to depth of a few kilometers. Further increases in pressure and temperature indicate stresses approximately constant. These  $P_C$  and  $T$  are characteristic of mid-crustal depths. The lab data suggests that strength reduction would then occur toward lower crust levels, where temperature favors dominantly plastic deformation. Note that the data at  $T = 20^{\circ}\text{C}$ - $P_C = 30\text{ MPa}$ ,  $T = 200^{\circ}\text{C}$ - $P_C = 200\text{ MPa}$ , and  $T = 300^{\circ}\text{C}$ - $P_C = 300\text{ MPa}$ , which represent  $T$ - $P_C$  conditions at a depth of  $z = 1, 8,$  and  $12\text{ km}$ , respectively, are those directly measured at lab strain rates (Tab. 1). For the data at  $T = 600^{\circ}\text{C}$  and  $650^{\circ}\text{C}$ , we used the strength measured at  $P_C = 300\text{ MPa}$  since the pressure sensitivity is very low at  $T \geq 600^{\circ}\text{C}$ . Also, strength at  $z = 4\text{ km}$  ( $T = 100^{\circ}\text{C}$ ,  $P_C = 100\text{ MPa}$ ) and  $z = 16\text{ km}$  ( $T = 400^{\circ}\text{C}$ ,  $P_C = 400\text{ MPa}$ ) were not directly measured in our tests. For the first, we extrapolated the strength measured at  $T = 200^{\circ}\text{C}$ ,  $P_C = 100\text{ MPa}$  to  $T = 100^{\circ}\text{C}$  from Figure 5c to estimate the strength at  $z = 4\text{ km}$ . For  $z = 16\text{ km}$ , we extrapolated the strength measured at  $T = 400^{\circ}\text{C}$  and  $P_C = 300\text{ MPa}$ , to  $T = 400^{\circ}\text{C}$  and  $P_C = 400\text{ MPa}$  using Figure 3c. Extrapolated data are shown by a smaller symbol size in Figure 12.

For the extrapolation to natural conditions, we need to consider the effect of strain due to hardening and of strain rate at high  $T$ . For an increase of strain from 0.05 to 0.10, the strength increases by about 13%–23% in the depth range of 4–16 km (open squares in Figure 12). Since the hardening coefficient decreases with increasing strain in this depth/temperature interval (Figure 2), we may expect that the strength reaches a peak at high strain. Torsion experiments on Carrara marble performed at  $T = 150$ – $350^{\circ}\text{C}$  and  $P_C = 400\text{ MPa}$  revealed peak strengths at shear strains of about 1–1.5 (equivalent to axial strains of about 0.5–0.7) (Rybacki et al., 2013). These peak strengths are about twice as high as the stress at a strain of 0.05 measured here. In contrast, at low  $T$  ( $\leq 150^{\circ}\text{C}$ ) and high  $T$  ( $\geq 600^{\circ}\text{C}$ ) stresses are not much influenced by total strain because the hardening coefficient is low (Figures 2 and 5). With these assumptions, the strength at laboratory strain rates, roughly shown in Figure 12 by the broken line labeled  $\Delta\sigma_{\text{max}@1 \times 10^{-5}\text{ s}^{-1}}$ , increases at mid-crustal depth.

Based on our lab measurements, the influence of strain rate on strength is expected to be negligible at low to intermediate temperatures ( $200^{\circ}\text{C} \leq T \leq 400^{\circ}\text{C}$ ) (Figures 4 and 5). Outside this temperature range the strength decreases with decreasing  $\dot{\epsilon}$ . Assuming a power law relation between stress and strain rate and taking average stress exponents of  $n = 45$  and  $n = 9.3$  for  $T = 20^{\circ}\text{C}$  and  $T = 600\text{--}700^{\circ}\text{C}$ , respectively (Figure 4c), the expected reduction of stress at  $\epsilon = 0.05$  and  $\dot{\epsilon} = 1 \times 10^{-14} \text{ s}^{-1}$  compared to that at  $1 \times 10^{-5} \text{ s}^{-1}$  is  $\approx 35\%$  at low  $T$  and  $\approx 85\%$  at high  $T$ . The resulting extrapolated stress profile is given approximately by the green broken line in Figure 12 (labeled  $\Delta\sigma_{0.05 @ 1 \times 10^{-14} \text{ s}^{-1}}$ ). However, this conclusion relies on the assumption that the strain rate insensitivity observed in our experiments at  $200^{\circ}\text{C} \leq T \leq 400^{\circ}\text{C}$  is also valid at natural strain rate and that the relative contribution of the three main deformation mechanisms do not change significantly. Based on these very speculative differential stress profiles, we may conclude that the BDT in terms of pressure dependence is close to  $\Delta\sigma = 4 P_c$  and the BPT more close to  $\Delta\sigma = 0.5 P_c$  (Figure 12).

It is worth mentioning that also the grain size affects the strength of calcite rocks at high  $T$  (e.g., Renner et al., 2002; Schmid et al., 1980) and, of course, we have not considered many other factors, for example, the influence of water as a pore fluid, the presence of pre-existing faults, or effect of porosity within the rocks.

Semi-brittle flow may mark the base of the seismogenic zone, probably characterized by velocity strengthening frictional behavior on preexisting faults (Burov, 2015; Chen & Molnar, 1983; Jackson, 2002; Molnar, 2020). Furthermore, the semi-brittle regime may be the source location of slow slip events and tremors (e.g., Fagereng et al., 2014; Reber et al., 2015). In calcite rocks, the slip stability is affected by pressure and temperature dependent processes (Aubry et al., 2020; Carpenter et al., 2016; Passelègue et al., 2019; Verberne et al., 2017; Verberne et al., 2015) and the rate dependence of the empirical rate-and-state friction law may be physically explained by the competition of brittle and plastic processes at contact asperities (e.g., Chen et al., 2021; Chen & Spiers, 2016; Verberne et al., 2017; Verberne et al., 2020). It is also conceivable that the state variable is affected by the hardening coefficient that evolves with strain and depends on the  $P_c$ - $T$  -  $\dot{\epsilon}$  conditions in the semi-brittle regime. It is therefore important to formulate a constitutive law for semi-brittle deformation to better constrain the depths, mechanical strength, and stability of faults when rocks deform in this regime at natural strain rates.

## 5. Conclusions

We performed a comprehensive set of triaxial deformation experiments on Carrara marble covering a wide range of temperatures, pressures and strain rates to explore the influence of thermodynamic boundary conditions on the mechanical behavior and associated evolution of microstructures in the semi-brittle deformation regime. We focused on obtaining mechanical data and qualitative microscopical observations. The results confirm earlier results suggesting that there is a complex interplay amongst the three main deformation mechanisms: cataclasis, twinning and dislocation activity. All these mechanisms are active under the entire range of conditions, but the partitioning of strain amongst the three mechanisms varies as  $P_c$ ,  $T$ , and strain rate change.

Twinning has a strong effect on sample strength even though twinning occurs with lowest CRSS. Hardening coefficients and twinning are co-related, and the mechanical results are consistent with a “dynamic Hall-Petch” relation, suggesting that the twin structure influences the dislocation mean free path or the dislocation forest structure. Hardening of grains that twin easily may be responsible for distribution of strain to new grains, preventing strain localization, thus, prolonging semi-brittle deformation. The hardening coefficient at intermediate temperatures is large (several per cent of the shear modulus). This deformation in dense marble rocks is similar to that seen in TWIP metals.

The partitioning of strain among the different deformation processes changes in a complex way with changes in temperature, pressure, and strain rate, perhaps reflecting changing microphysics in the way that separate mechanisms accommodate strain heterogeneities. Microfracturing is favored at low  $T$ , high  $\dot{\epsilon}$ , and low  $P_c$ . Conversely, crystal plasticity predominates at high  $T$ , low  $\dot{\epsilon}$ , and high  $P_c$ . Surprisingly, at  $T \approx 200\text{--}400^{\circ}\text{C}$ , the variation of strength and hardening coefficient with strain rate and pressure is lower than at other  $T$ . Understanding the variations in this region will be key to formulating a more rigorous prediction of natural deformation in the semi-brittle regime.

Currently, no microphysically-based constitutive law is available to describe semi-brittle behavior and even the transition from semi-brittle to fully plastic deformation is poorly constrained by the existing empirical estimates.

However, it can be expected that under natural conditions in the Earth's crust the strength of marbles is mainly governed by semi-brittle deformation over a large depth extent, and that there may be regions where strength is influenced more by total strain than by changes in strain rate.

## Data Availability Statement

Original (averaged stress-strain) data of all samples can be accessed via FTP from the GFZ data repository (<https://doi.org/10.5880/GFZ.4.2.2021.003>).

## Acknowledgments

We would like to thank the editor, as well as Gabriel Meyer and another anonymous reviewer for detailed comments that improved the clarity of the manuscript. We thank Michael Naumann for help with experiments, Stefan Gehrmann for sample and thin section preparation, and the SEM-TEM staff at MIT for assistance in electronic microscopy. We have benefited from fruitful discussions with Luiz Morales. L.N. was supported by CSC scholarship. Some of the early experiments were done while BE held a von Humboldt fellowship at the GFZ.

## References

- Alheid, H. (1981). *Untersuchung von Bruch- und Scherprozessen im Granit und Serpentin bei hohen Drücken und Temp.* Berchem Institute of Geophysics.
- Ardejan, M., Beyerlein, I. J., McWilliams, B. A., & Knezevic, M. (2016). Strain rate and temperature sensitive multi-level crystal plasticity model for large plastic deformation behavior: Application to AZ31 magnesium alloy. *International Journal of Plasticity*, 83, 90–109. <https://doi.org/10.1016/j.ijplas.2016.04.005>
- Arul Kumar, M., Beyerlein, I. J., & Tomé, C. N. (2016). Effect of local stress fields on twin characteristics in HCP metals. *Acta Materialia*, 116, 143–154. <https://doi.org/10.1016/j.actamat.2016.06.042>
- Arul Kumar, M., Kanjarla, A. K., Niezgodá, S. R., Lebensohn, R. A., & Tomé, C. N. (2015). Numerical study of the stress state of a deformation twin in magnesium. *Acta Materialia*, 84, 349–358. <https://doi.org/10.1016/j.actamat.2014.10.048>
- Ashby, M., & Hallam, S. (1986). The failure of brittle solids containing small cracks under compressive stress states. *Acta Metallurgica*, 34, 497–510. [https://doi.org/10.1016/0001-6160\(86\)90086-6](https://doi.org/10.1016/0001-6160(86)90086-6)
- Ashby, M. F. (1970). The deformation of plastically non-homogeneous materials. *The Philosophical Magazine: A Journal of Theoretical Experimental and Applied Physics*, 21(170), 399–424. <https://doi.org/10.1080/14786437008238426>
- Ashby, M. F., Gandhi, C., & Taplin, D. M. R. (1979). Overview No. 3 Fracture-mechanism maps and their construction for f.c.c. metals and alloys. *Acta Metallurgica*, 27(5), 699–729. [https://doi.org/10.1016/0001-6160\(79\)90105-6](https://doi.org/10.1016/0001-6160(79)90105-6)
- Atkinson, B. K. (1984). Sub-critical crack growth in geologic materials. *Journal of Geophysical Research*, 89, 4077–4113. <https://doi.org/10.1029/jb089ib06p04077>
- Atkinson, B. K., & Avdis, V. (1980). Fracture mechanics parameters of some rock-forming minerals determined using an indentation technique. *International Journal of Rock Mechanics and Mining Sciences & Geomechanics Abstracts*, 17(6), 383–386. [https://doi.org/10.1016/0148-9062\(80\)90523-9](https://doi.org/10.1016/0148-9062(80)90523-9)
- Aubry, J., Passelegue, F. X., Escartin, J., Gasc, J., Deldicque, D., & Schubnel, A. (2020). Fault stability across the seismogenic zone. *Journal of Geophysical Research-Solid Earth*, 125(8), e2020JB019670. <https://doi.org/10.1029/2020JB019670>
- Babai, H. A., & La Tour, T. E. (1994). Semibrittle and cataclastic deformation of hornblende-quartz rocks in a ductile shear zone. *Tectonophysics*, 229, 19–30. [https://doi.org/10.1016/0040-1951\(94\)90003-5](https://doi.org/10.1016/0040-1951(94)90003-5)
- Barber, D. J., & Wenk, H. R. (1979). Deformation twinning in calcite, dolomite, and other rhombohedral carbonates. *Physics and Chemistry of Minerals*, 5(2), 141–165. <https://doi.org/10.1007/bf00307550>
- Barber, D. J., Wenk, H. R., Gomez-Barreiro, J., Rybacki, E., & Dresen, G. (2007). Basal slip and texture development in calcite: New results from torsion experiments. *Physics and Chemistry of Minerals*, 34(2), 73–84. <https://doi.org/10.1007/s00269-006-0129-3>
- Barnhoorn, A., Bystricky, M., Burlini, L., & Kunze, K. (2004). The role of recrystallisation on the deformation behaviour of calcite rocks: Large strain torsion experiments on Carrara marble. *Journal of Structural Geology*, 26(5), 885–903. <https://doi.org/10.1016/j.jsg.2003.11.024>
- Beall, A., Fagereng, A., & Ellis, S. (2019). Fracture and weakening of jammed subduction shear zones, leading to the generation of slow slip events. *Geochemistry Geophysics Geosystems*, 20(11), 4869–4884. <https://doi.org/10.1029/2019gc008481>
- Beyerlein, I. J., & Tome, C. N. (2008). A dislocation-based constitutive law for pure Zr including temperature effects. *International Journal of Plasticity*, 24(5), 867–895. <https://doi.org/10.1016/j.ijplas.2007.07.017>
- Bos, B., & Spiers, C. J. (2002). Frictional-viscous flow of phyllosilicate-bearing fault rock: Microphysical model and implications for crustal strength profiles. *Journal of Geophysical Research*, 107(B2), 2028. <https://doi.org/10.1029/2001JB000301>
- Bouaziz, O. (2012). Strain-hardening of twinning-induced plasticity steels. *Scripta Materialia*, 66(12), 982–985. <https://doi.org/10.1016/j.scriptamat.2011.11.029>
- Bouaziz, O., Allain, S., & Scott, C. (2008). Effect of grain and twin boundaries on the hardening mechanisms of twinning-induced plasticity steels. *Scripta Materialia*, 58(6), 484–487. <https://doi.org/10.1016/j.scriptamat.2007.10.050>
- Bouaziz, O., & Guelton, N. (2001). Modelling of TWIP effect on work-hardening. *Materials Science and Engineering a-Structural Materials Properties Microstructure and Processing*, 319, 246–249. [https://doi.org/10.1016/S0921-5093\(00\)02019-0](https://doi.org/10.1016/S0921-5093(00)02019-0)
- Brace, W. F., & Kohlstedt, D. L. (1980). Limits on lithospheric stress imposed by laboratory experiments. *Journal of Geophysical Research: Solid Earth*, 85(B11), 6248–6252. <https://doi.org/10.1029/JB085iB11p06248>
- Brace, W. F., & Walsh, J. B. (1962). Some direct measurements of the surface energy of quartz and orthoclase. *American Mineralogist*, 47(9–10), 1111.
- Brantut, N., Baud, P., Heap, M. J., & Meredith, P. G. (2012). Micromechanics of brittle creep in rocks. *Journal of Geophysical Research*, 117(B8), B08412. <https://doi.org/10.1029/2012jb009299>
- Brantut, N., Heap, M. J., Baud, P., & Meredith, P. G. (2014). Mechanisms of time-dependent deformation in porous limestone. *Journal of Geophysical Research-Solid Earth*, 119(7), 5444–5463. <https://doi.org/10.1002/2014jb011186>
- Brantut, N., Heap, M. J., Meredith, P. G., & Baud, P. (2013). Time-dependent cracking and brittle creep in crustal rocks: A review. *Journal of Structural Geology*, 52(0), 17–43. <https://doi.org/10.1016/j.jsg.2013.03.007>
- Brantut, N., Schubnel, A., & Gueguen, Y. (2011). Damage and rupture dynamics at the brittle-ductile transition: The case of gypsum. *Journal of Geophysical Research*, 116(B1), B01404. <https://doi.org/10.1029/2010jb007675>
- Brown, D. W., Beyerlein, I. J., Sisneros, T. A., Clausen, B., & Tome, C. N. (2012). Role of twinning and slip during compressive deformation of beryllium as a function of strain rate. *International Journal of Plasticity*, 29, 120–135. <https://doi.org/10.1016/j.ijplas.2011.08.006>



- Brown, L. M., & Clarke, D. R. (1975). Work hardening due to internal stresses in composite materials. *Acta Metallurgica*, 23, 821–830. [https://doi.org/10.1016/0001-6160\(75\)90198-4](https://doi.org/10.1016/0001-6160(75)90198-4)
- Broz, M. E., Cook, R. F., & Whitney, D. L. (2006). Microhardness, toughness, and modulus of Mohs scale minerals. *American Mineralogist*, 91(1), 135–142. <https://doi.org/10.2138/am.2006.1844>
- Bruijn, R. H. C., Kunze, K., Mainprice, D., & Burlini, L. (2011). Mechanical and microstructural development of Carrara marble with pre-existing strain variation. *Tectonophysics*, 503(1–2), 75–91. <https://doi.org/10.1016/j.tecto.2010.09.029>
- Bürgmann, R., & Dresen, G. (2008). Rheology of the lower crust and upper mantle: Evidence from rock mechanics, geodesy, and field observations. *Annual Review of Earth and Planetary Sciences*, 36(1), 531–567. <https://doi.org/10.1146/annurev.earth.36.031207.124326>
- Burkhard, M. (1993). Calcite twins, their geometry, appearance and significance as stress-strain markers and indicators of tectonic regime - A review. *Journal of Structural Geology*, 15(3–5), 351–368. [https://doi.org/10.1016/0191-8141\(93\)90132-T](https://doi.org/10.1016/0191-8141(93)90132-T)
- Burov, E. B. (2015). Plate rheology and mechanics. In A. B. Watts (Ed.), *Treatise on geophysics* (2nd ed., Vol. 6, pp. 95–152). Elsevier. <https://doi.org/10.1016/b978-0-444-53802-4.00112-3>
- Byerlee, J. (1968). Brittle-ductile transition in rocks. *Journal of Geophysical Research*, 73, 4741–4750. <https://doi.org/10.1029/jb073i014p04741>
- Carmichael, R. S. (Ed.). (1989). *Practical handbook of physical properties of rocks and minerals*. CRC.
- Carpenter, B. M., Ikari, M. J., & Marone, C. (2016). Laboratory observations of time-dependent frictional strengthening and stress relaxation in natural and synthetic fault gouges. *Journal of Geophysical Research-Solid Earth*, 121(2), 1183–1201. <https://doi.org/10.1002/2015jb012136>
- Carter, N., & Kirby, S. (1978). Transient creep and semibrittle behavior of crystalline rocks. *Pure and Applied Geophysics*, 116, 807–839. <https://doi.org/10.1007/bf00876540>
- Charles, R. J. (1958). Static fatigue of Glass. I. *Journal of Applied Physics*, 29(11), 1549–1553. <https://doi.org/10.1063/1.1722991>
- Chen, J., Niemeijer, A. R., & Spiers, C. J. (2021). Microphysical modeling of carbonate fault friction at slip rates spanning the full seismic cycle. *Journal of Geophysical Research: Solid Earth*, 126(3), e2020JB021024. <https://doi.org/10.1029/2020JB021024>
- Chen, J. Y., & Spiers, C. J. (2016). Rate and state frictional and healing behavior of carbonate fault gouge explained using microphysical model. *Journal of Geophysical Research-Solid Earth*, 121(12), 8642–8665. <https://doi.org/10.1002/2016jb013470>
- Chen, W., & Molnar, P. (1983). Focal depth of intracontinental and intraplate earthquakes and their implications for the thermal and mechanical properties of the lithosphere. *Journal of Geophysical Research*, 88, 4183–4214. <https://doi.org/10.1029/jb088i05p04183>
- Chester, F. (1988). The brittle-ductile transition in a deformation-mechanism map for halite. *Tectonophysics*, 154, 125–136. [https://doi.org/10.1016/0040-1951\(88\)90230-2](https://doi.org/10.1016/0040-1951(88)90230-2)
- Cordero, Z. C., Knight, B. E., & Schuh, C. A. (2016). Six decades of the Hall-Petch effect - A survey of grain-size strengthening studies on pure metals. *International Materials Reviews*, 61(8), 495–512. <https://doi.org/10.1080/09506608.2016.1191808>
- Covey-Crump, S. J. (1994). The application of Hart's state variable description of inelastic deformation to Carrara marble at T <450°C. *Journal of Geophysical Research*, 99, 19793–19808. <https://doi.org/10.1029/94jb01797>
- Covey-Crump, S. J. (1998). Evolution of mechanical state in Carrara marble during deformation at 400° to 700°C. *Journal of Geophysical Research*, 103(B12), 29781–29794. <https://doi.org/10.1029/1998jb900005>
- Covey-Crump, S. J. (2001). Variation of the exponential and power law creep parameters with strain for Carrara marble deformed at 120 degrees to 400 degrees C. *Geophysical Research Letters*, 28(12), 2301–2304. <https://doi.org/10.1029/2000gl012692>
- Covey-Crump, S. J., Schofield, P. F., & Oliver, E. C. (2017). Using neutron diffraction to examine the onset of mechanical twinning in calcite rocks. *Journal of Structural Geology*, 100, 77–97. <https://doi.org/10.1016/j.jsg.2017.05.009>
- Covey-Crump, S. J., Xiao, W. F., Mecklenburgh, J., Rutter, E. H., & May, S. E. (2016). Exploring the influence of loading geometry on the plastic flow properties of geological materials: Results from combined torsion plus axial compression tests on calcite rocks. *Journal of Structural Geology*, 88, 20–31. <https://doi.org/10.1016/j.jsg.2016.04.007>
- de Bresser, J. H. P. (1996). Steady state dislocation densities in experimentally deformed calcite materials: Single crystals versus polycrystals. *Journal of Geophysical Research*, 101(B10), 22189–22202. <https://doi.org/10.1029/96jb01759>
- de Bresser, J. H. P. (2002). On the mechanism of dislocation creep of calcite at high temperature: Inferences from experimentally measured pressure sensitivity and strain rate sensitivity of flow stress. *Journal of Geophysical Research*, 107(B12), 2337. <https://doi.org/10.1029/2002JB001812>
- de Bresser, J. H. P., & Spiers, C. J. (1993). Slip systems in calcite single crystals deformed at 300–800°C. *Journal of Geophysical Research*, 98(B4), 6397–6409. <https://doi.org/10.1029/92jb02044>
- de Bresser, J. H. P., & Spiers, C. J. (1997). Strength characteristics of the r, f, and c slip systems in calcite. *Tectonophysics*, 272(1), 1–23. [https://doi.org/10.1016/s0040-1951\(96\)00273-9](https://doi.org/10.1016/s0040-1951(96)00273-9)
- de Bresser, J. H. P., Urai, J. L., & Olgaard, D. L. (2005). Effect of water on the strength and microstructure of Carrara marble axially compressed at high temperature. *Journal of Structural Geology*, 27(2), 265–281. <https://doi.org/10.1016/j.jsg.2004.10.002>
- De Cooman, B. C., Estrin, Y., & Kim, S. K. (2018). Twinning-induced plasticity (TWIP) steels. *Acta Materialia*, 142, 283–362. <https://doi.org/10.1016/j.actamat.2017.06.046>
- Dell'Angelo, L. N., & Tullis, J. (1996). Textural and mechanical evolution with progressive strain in experimentally deformed aplites. *Tectonophysics*, 256(1–4), 57–82. [https://doi.org/10.1016/0040-1951\(95\)00166-2](https://doi.org/10.1016/0040-1951(95)00166-2)
- Dimanov, A., Rybacki, E., Wirth, R., & Dresen, G. (2007). Creep and strain-dependent microstructures of synthetic anorthite-diopside aggregates. *Journal of Structural Geology*, 29(6), 1049–1069. <https://doi.org/10.1016/j.jsg.2007.02.010>
- Ding, J., Chester, F. M., Chester, J. S., Shen, X., & Arson, C. (2021). Coupled brittle and viscous micromechanisms produce semibrittle flow, grain-boundary sliding, and anelasticity in salt-rock. *Journal of Geophysical Research-Solid Earth*, 126(2), e2020JB021261. <https://doi.org/10.1029/2020JB021261>
- Dresen, G., Duyster, J., Stockhert, B., Wirth, R., & Zulauf, G. (1997). Quartz dislocation microstructure between 7000 m and 9100 m depth from the Continental Deep Drilling Program KTB. *Journal of Geophysical Research-Solid Earth*, 102(B8), 18443–18452. <https://doi.org/10.1029/96jb03394>
- Edmond, J., & Paterson, M. (1972). Volume changes during the deformation of rocks at high pressures. *International Journal of Rock Mechanics and Mining Sciences and Geomechanics Abstracts*, 9, 161–182. [https://doi.org/10.1016/0148-9062\(72\)90019-8](https://doi.org/10.1016/0148-9062(72)90019-8)
- Estrin, Y., & Kubin, L. P. (1986). Local strain hardening and nonuniformity of plastic deformation. *Acta Metallurgica*, 34(12), 2455–2464. [https://doi.org/10.1016/0001-6160\(86\)90148-3](https://doi.org/10.1016/0001-6160(86)90148-3)
- Evans, B., Fredrich, J., & Wong, T.-F. (1990). The Brittle-Ductile transition in rocks: Recent experimental and theoretical progress. In *The Heard*. (Vol. 56, pp. 1–20). American Geophysical Union Geophysical Monography. <https://doi.org/10.1029/gm056p0001>
- Fagereng, A., Hillary, G. W. B., & Diener, J. F. A. (2014). Brittle-viscous deformation, slow slip, and tremor. *Geophysical Research Letters*, 41(12), 4159–4167. <https://doi.org/10.1002/2014gl060433>
- Ferguson, C. C. (1983). Composite flow laws derived from high temperature experimental data on limestone and marble. *Tectonophysics*, 95(3–4), 253–266. [https://doi.org/10.1016/0040-1951\(83\)90071-9](https://doi.org/10.1016/0040-1951(83)90071-9)

- Ferrill, D. A. (1998). Critical re-evaluation of differential stress estimates from calcite twins in coarse-grained limestone. *Tectonophysics*, 285(1–2), 77–86. [https://doi.org/10.1016/S0040-1951\(97\)00190-X](https://doi.org/10.1016/S0040-1951(97)00190-X)
- Ferrill, D. A., Morris, A. P., Evans, M. A., Burkhard, M., Groshong, R. H., & Onasch, C. M. (2004). Calcite twin morphology: A low-temperature deformation geothermometer. *Journal of Structural Geology*, 26(8), 1521–1529. <https://doi.org/10.1016/j.jsg.2003.11.028>
- Fischer, G., & Paterson, M. (1989). Dilatancy during rock deformation at high temperatures and pressures. *Journal of Geophysical Research*, 94, 17607–17617. <https://doi.org/10.1029/jb094ib12p17607>
- Fredrich, J., Evans, B., & Wong, T.-F. (1989). Micromechanics of the brittle to plastic transition in Carrara marble. *Journal of Geophysical Research*, 94(B4), 4129–4145. <https://doi.org/10.1029/jb094ib04p04129>
- Gapais, D. (1989). Shear structures within deformed granites: Mechanical and thermal indicators. *Geology*, 17(12), 1144–1147. [https://doi.org/10.1130/0091-7613\(1989\)017<1144:sswdgm>2.3.co;2](https://doi.org/10.1130/0091-7613(1989)017<1144:sswdgm>2.3.co;2)
- Gil Sevillano, J., & de las Cuevas, F. (2012). Internal stresses and the mechanism of work hardening in twinning-induced plasticity steels. *Scripta Materialia*, 66(12), 978–981. <https://doi.org/10.1016/j.scriptamat.2012.02.019>
- Gilman, J. J. (1960). Direct measurements of the surface energies of crystals. *Journal of Applied Physics*, 31(12), 2208–2218. <https://doi.org/10.1063/1.1735524>
- Goetze, C., & Evans, B. (1979). Stress and temperature in the bending lithosphere as constrained by experimental rock mechanics. *Geophysical Journal International*, 59(3), 463–478. <https://doi.org/10.1111/j.1365-246X.1979.tb02567.x>
- Gowd, T., & Rummel, F. (1980). Effect of confining pressure on the fracture behaviour of a porous rock. *International Journal of Rock Mechanics and Mining Sciences and Geomechanics Abstracts*, 17, 225–229. [https://doi.org/10.1016/0148-9062\(80\)91089-x](https://doi.org/10.1016/0148-9062(80)91089-x)
- Guéry, A. A.-C., Cormery, F., Shao, J. F., & Kondo, D. (2008). A micromechanical model of elastoplastic and damage behavior of a cohesive geomaterial. *International Journal of Solids and Structures*, 45(5), 1406–1429. <https://doi.org/10.1016/j.ijsolstr.2007.09.025>
- Gupta, Y. P., & Santhanam, A. T. (1969). On cleavage surface energy of calcite crystals. *Acta Metallurgica*, 17, 419–424. [https://doi.org/10.1016/0001-6160\(69\)90022-4](https://doi.org/10.1016/0001-6160(69)90022-4)
- Haimson, B. (2006). True triaxial stresses and the brittle fracture of rock. *Pure and Applied Geophysics*, 163(5–6), 1101–1130. <https://doi.org/10.1007/s00024-006-0065-7>
- Handy, M. R., Wissing, S. B., & Streit, L. E. (1999). Frictional-viscous flow in mylonite with varied biminerale composition and its effect on lithospheric strength. *Tectonophysics*, 303, 175–191. [https://doi.org/10.1016/S0040-1951\(98\)00251-0](https://doi.org/10.1016/S0040-1951(98)00251-0)
- Hart, E. (1970). A phenomenological theory for plastic deformation of polycrystalline metals. *Acta Metallurgica*, 18, 599–202. [https://doi.org/10.1016/0001-6160\(70\)90089-1](https://doi.org/10.1016/0001-6160(70)90089-1)
- Hart, E. (1976). Constitutive relations for the nonelastic deformation of metals. *Journal of Engineering Materials & Technology*, 98, 193–200. <https://doi.org/10.1115/1.3443368>
- Heard, H. (1960). Transition from brittle fracture to ductile flow in Solenhofen Limestone as a function of temperature, confining pressure, and interstitial fluid pressure. *Geological Society of America: Memoirs*, 79, 193–226. <https://doi.org/10.1130/mem79-p193>
- Henry, J. P., Paquet, J., & Tancrez, J. P. (1977). Experimental study of crack propagation in calcite rocks. *International Journal of Rock Mechanics and Mining Sciences & Geomechanics Abstracts*, 14(2), 85–91. [https://doi.org/10.1016/0148-9062\(77\)90200-5](https://doi.org/10.1016/0148-9062(77)90200-5)
- Herrmann, J., Rybacki, E., Sone, H., & Dresen, G. (2018). Deformation experiments on Bowland and Posidonia Shale—Part I: Strength and young’s modulus at ambient and in situ  $P_c$ – $T$  conditions. *Rock Mechanics and Rock Engineering*, 51(12), 3645–3666. <https://doi.org/10.1007/s00603-018-1572-4>
- Horii, H., & Nemat-Nasser, S. (1986). Brittle failure in compression - Splitting, faulting and brittle-ductile transition. *Philosophical Transactions Royal Society London Series a-Mathematical Physical and Engineering Science*, 319(1549), 337–374.
- Hou, R. B., Zhang, K., Tao, J., Xue, X. R., & Chen, Y. L. (2019). A nonlinear creep damage coupled model for rock considering the effect of initial damage. *Rock Mechanics and Rock Engineering*, 52(5), 1275–1285. <https://doi.org/10.1007/s00603-018-1626-7>
- Hucka, V., & Das, B. (1974). Brittleness determination of rocks by different methods. *International Journal of Rock Mechanics and Mining Sciences and Geomechanics Abstracts*, 11, 389–392. [https://doi.org/10.1016/0148-9062\(74\)91109-7](https://doi.org/10.1016/0148-9062(74)91109-7)
- Jackson, J. (2002). Strength of the continental lithosphere: Time to abandon the jelly sandwich? *Geological Society of America: Publication*, 9(2), 4–10. [https://doi.org/10.1130/1052-5173\(2002\)012<0004:sotclt>2.0.co;2](https://doi.org/10.1130/1052-5173(2002)012<0004:sotclt>2.0.co;2)
- Jamison, W. R., & Spang, J. H. (1976). Use of calcite twin lamellae to infer differential stress. *The Geological Society of America Bulletin*, 87(6), 868–872. [https://doi.org/10.1130/0016-7606\(1976\)87<868:uocltt>2.0.co;2](https://doi.org/10.1130/0016-7606(1976)87<868:uocltt>2.0.co;2)
- Jammes, S., Lavier, L. L., & Reber, J. E. (2015). Localization and delocalization of deformation in a biminerale material. *Journal of Geophysical Research-Solid Earth*, 120(5), 3649–3663. <https://doi.org/10.1002/2015jb011890>
- Kaga, H., & Gilman, J. J. (1969). Twinning and detwinning in calcite. *Journal of Applied Physics*, 40(8), 3196–3207. <https://doi.org/10.1063/1.1658166>
- Kamali-Asl, A., Ghazanfari, E., Newell, P., & Stevens, M. (2018). Elastic, viscoelastic, and strength properties of Marcellus Shale specimens. *Journal of Petroleum Science and Engineering*, 171, 662–679. <https://doi.org/10.1016/j.petrol.2018.05.074>
- Karato, S. (2008). *Deformation of earth materials*. Cambridge University Press.
- Kirby, S., & Kronenberg, A. (1984). Deformation of clinopyroxenite: Evidence for a transition in flow mechanisms and semibrittle behavior. *Journal of Geophysical Research*, 89, 3177–3192. <https://doi.org/10.1029/jb089ib05p03177>
- Kirby, S. H. (1980). Tectonic stresses in the lithosphere: Constraints provided by the experimental deformation of rocks. *Journal of Geophysical Research: Solid Earth*, 85(B11), 6353–6363. <https://doi.org/10.1029/JB085B11p06353>
- Kocks, U. F., & Mecking, H. (2003). Physics and phenomenology of strain hardening: The FCC case. *Progress in Materials Science*, 48(3), 171–273. [https://doi.org/10.1016/S0079-6425\(02\)00003-8](https://doi.org/10.1016/S0079-6425(02)00003-8)
- Kohlstedt, D. L., Evans, B., & Mackwell, S. J. (1995). Strength of the lithosphere - constraints imposed by laboratory experiments. *Journal of Geophysical Research-Solid Earth*, 100(B9), 17587–17602. <https://doi.org/10.1029/95jb01460>
- Lacombe, O. (2007). Comparison of paleostress magnitudes from calcite twins with contemporary stress magnitudes and frictional sliding criteria in the continental crust: Mechanical implications. *Journal of Structural Geology*, 29(1), 86–99. <https://doi.org/10.1016/j.jsg.2006.08.009>
- Lacombe, O., & Laurent, P. (1992). Determination of principal stress magnitudes using calcite twins and rock mechanics data. *Tectonophysics*, 202(1), 83–93. [https://doi.org/10.1016/0040-1951\(92\)90456-G](https://doi.org/10.1016/0040-1951(92)90456-G)
- Laurent, P., Kern, H., & Lacombe, O. (2000). Determination of deviatoric stress tensors based on inversion of calcite twin data from experimentally deformed monophase samples. Part II. Axial and triaxial stress experiments. *Tectonophysics*, 327, 131–148. [https://doi.org/10.1016/S0040-1951\(00\)00165-7](https://doi.org/10.1016/S0040-1951(00)00165-7)
- Lavier, L. L., Bennett, R. A., & Duddu, R. (2013). Creep events at the brittle ductile transition. *Geochemistry Geophysics Geosystems*, 14(9), 3334–3351. <https://doi.org/10.1002/ggge.20178>



- Lebensohn, R. A., & Tome, C. N. (1993). A self-consistent anisotropic approach for the simulation of plastic-deformation and texture development of polycrystals - Application to zirconium alloys. *Acta Metallurgica et Materialia*, 41(9), 2611–2624. [https://doi.org/10.1016/0956-7151\(93\)90130-K](https://doi.org/10.1016/0956-7151(93)90130-K)
- Lyakhovskiy, V., Zhu, W. L., & Shalev, E. (2015). Visco-poroelastic damage model for brittle-ductile failure of porous rocks. *Journal of Geophysical Research-Solid Earth*, 120(4), 2179–2199. <https://doi.org/10.1002/2014jb011805>
- McLaren, A. C., & Pryer, L. L. (2001). Microstructural investigation of the interaction and interdependence of cataclastic and plastic mechanisms in Feldspar crystals deformed in the semi-brittle field. *Tectonophysics*, 335(1–2), 1–15. [https://doi.org/10.1016/S0040-1951\(01\)00042-7](https://doi.org/10.1016/S0040-1951(01)00042-7)
- Meyer, G. G., Brantut, N., Mitchell, T. M., & Meredith, P. G. (2019). Fault reactivation and strain partitioning across the brittle-ductile transition. *Geology*, 47(12), 1127–1130. <https://doi.org/10.1130/G46516.1>
- Molnar, P. (2020). The Brittle-Plastic transition, earthquakes, temperatures, and strain rates. *Journal of Geophysical Research-Solid Earth*, 125(7), e2019JB019335. <https://doi.org/10.1029/2019JB019335>
- Morales, L. F. G., Lloyd, G. E., & Mainprice, D. (2014). Fabric transitions in quartz via viscoplastic self-consistent modeling part I: Axial compression and simple shear under constant strain. *Tectonophysics*, 636, 52–69. <https://doi.org/10.1016/j.tecto.2014.08.011>
- Nardini, L., Rybacki, E., Dohmann, M. J. E. A., Morales, L. F. G., Brune, S., & Dresen, G. (2018). High-temperature shear zone formation in Carrara marble: The effect of loading conditions. *Tectonophysics*, 749, 120–139. <https://doi.org/10.1016/j.tecto.2018.10.022>
- Nardini, L., Rybacki, E., Krause, M., Morales, L. F. G., & Dresen, G. (2020). Control of the geometric arrangement of material heterogeneities on strain localization at the brittle-to-ductile transition in experimentally deformed carbonate rocks. *Journal of Structural Geology*, 135, 104038. <https://doi.org/10.1016/j.jsg.2020.104038>
- Nicolas, A., Fortin, J., & Gueguen, Y. (2017). Micromechanical constitutive model for low-temperature constant strain rate deformation of limestones in the brittle and semi-brittle regime. *Geophysical Journal International*, 211(1), 300–321. <https://doi.org/10.1093/gji/ggx299>
- Niemeijer, A. R., & Spiers, C. J. (2007). A microphysical model for strong velocity weakening in phyllosilicate-bearing fault gouges. *Journal of Geophysical Research*, 112(B10), B10405. <https://doi.org/10.1029/2007jb005008>
- Noda, H., & Shimamoto, T. (2010). A rate- and state-dependent ductile flow law of polycrystalline halite under large shear strain and implications for transition to brittle deformation. *Geophysical Research Letters*, 37(9), L09310. <https://doi.org/10.1029/2010gl042512>
- Odedra, A., Ohnaka, M., Mochizuki, H., & Sammonds, P. (2001). Temperature and pore pressure effects on the shear strength of granite in the brittle-plastic transition regime. *Geophysical Research Letters*, 28(15), 3011–3014. <https://doi.org/10.1029/2001gl013321>
- Okazaki, K., Burdette, E., & Hirth, G. (2021). Rheology of the fluid oversaturated fault zones at the brittle-plastic transition. *Journal of Geophysical Research-Solid Earth*, 126(2), e2020JB020804. <https://doi.org/10.1029/2020JB020804>
- Parisio, F., & Laloui, L. (2017). Plastic-damage modeling of saturated quasi-brittle shales. *International Journal of Rock Mechanics and Mining Sciences*, 93, 295–306. <https://doi.org/10.1016/j.ijrmms.2017.01.016>
- Parisio, F., Samat, S., & Laloui, L. (2015). Constitutive analysis of shale: A coupled damage plasticity approach. *International Journal of Solids and Structures*, 75–76, 88–98. <https://doi.org/10.1016/j.ijsolstr.2015.08.003>
- Parlangeau, C., Dimanov, A., Lacombe, O., Hallais, S., & Daniel, J. M. (2019). Uniaxial compression of calcite single crystals at room temperature: Insights into twinning activation and development. *Solid Earth*, 10(1), 307–316. <https://doi.org/10.5194/se-10-307-2019>
- Parlangeau, C., Lacombe, O., Lucas, I., Kohler, J.-M., Daniel, J. M., & Schueller, S. (2018). *Is EBSD a more efficient tool than universal stage to collect calcite twin data as used in calcite twin inversion for stress*. Paper presented at the European Geological Union.
- Parlangeau, C., Lacombe, O., Schueller, S., & Daniel, J. M. (2018). Inversion of calcite twin data for paleostress orientations and magnitudes: A new technique tested and calibrated on numerically-generated and natural data. *Tectonophysics*, 722, 462–485. <https://doi.org/10.1016/j.tecto.2017.09.023>
- Passelègue, F. X., Aubry, J., Nicolas, A., Fondriest, M., Deldicque, D., Schubnel, A., et al. (2019). From fault creep to slow and fast earthquakes in carbonates. *Geology*, 47(8), 744–748. <https://doi.org/10.1130/g45868.1>
- Paterson, M. S. (1970). A high-pressure, high temperature apparatus for rock deformation. *International Journal of Rock Mechanics and Mining Sciences*, 7, 517–526. [https://doi.org/10.1016/0148-9062\(70\)90004-5](https://doi.org/10.1016/0148-9062(70)90004-5)
- Paterson, M. S. (1985). Dislocations and geologic deformation. In T. I. O. Metals (Ed.), *Dislocations properties in real materials* (pp. 359–375).
- Paterson, M. S., & Olgaard, D. L. (2000). Rock deformation tests to large shear strains in torsion. *Journal of Structural Geology*, 22(9), 1341–1358. [https://doi.org/10.1016/S0191-8141\(00\)00042-0](https://doi.org/10.1016/S0191-8141(00)00042-0)
- Paterson, M. S., & Wong, T.-f. (2005). *Experimental rock deformation - the brittle field* (2nd ed.). Springer Verlag.
- Pec, M., Stunitz, H., Heilbronner, R., & Drury, M. (2016). Semi-brittle flow of granitoid fault rocks in experiments. *Journal of Geophysical Research-Solid Earth*, 121(3), 1677–1705. <https://doi.org/10.1002/2015jb012513>
- Pieri, M., Burlini, L., Kunze, K., Stretton, I., & Olgaard, D. L. (2001). Rheological and microstructural evolution of Carrara marble with high shear strain: Results from high temperature torsion experiments. *Journal of Structural Geology*, 23(9), 1393–1413. [https://doi.org/10.1016/S0191-8141\(01\)00006-2](https://doi.org/10.1016/S0191-8141(01)00006-2)
- Pieri, M., Kunze, K., Burlini, L., Stretton, I., Olgaard, D. L., Burg, J. P., et al. (2001). Texture development of calcite by deformation and dynamic recrystallization at 1000 K during torsion experiments of marble to large strains. *Tectonophysics*, 330(1–2), 119–140. [https://doi.org/10.1016/S0040-1951\(00\)00225-0](https://doi.org/10.1016/S0040-1951(00)00225-0)
- Quintanilla-Terminel, A., & Evans, B. (2016). Heterogeneity of inelastic strain during creep of Carrara marble: Microscale strain measurement technique. *Journal of Geophysical Research-Solid Earth*, 121(8), 5736–715. <https://doi.org/10.1002/2016jb012970>
- Reber, J. E., Lavier, L. L., & Hayman, N. W. (2015). Experimental demonstration of a semi-brittle origin for crustal strain transients. *Nature Geoscience*, 8(9), 712. <https://doi.org/10.1038/Ngeo2496>
- Reber, J. E., & Pec, M. (2018). Comparison of brittle- and viscous creep in quartzites: Implications for semi-brittle flow of rocks. *Journal of Structural Geology*, 113, 90–99. <https://doi.org/10.1016/j.jsg.2018.05.022>
- Regenauer-Lieb, K., Weinberg, R. F., & Rosenbaum, G. (2006). The effect of energy feedbacks on continental strength. *Nature*, 442(7098), 67–70. <https://doi.org/10.1038/nature04868>
- Renner, J., & Evans, B. (2002). Do calcite rocks obey the power law creep equation? In S. de Meer, M. R. Drury, J. H. P. de Bresser, & G. Pennock (Eds.), *Deformation mechanisms, rheology, tectonics, current status future perspectives* (Vol. Special Publication 200, pp. 6–1). Geology Society of London.
- Renner, J., Evans, B., & Siddiqi, G. (2002). Dislocation creep of calcite. *Journal of Geophysical Research*, 107(B12), 2364. <https://doi.org/10.1029/2001jb001680>
- Richter, B., Stunitz, H., & Heilbronner, R. (2018). The brittle-to-viscous transition in polycrystalline quartz: An experimental study. *Journal of Structural Geology*, 114, 1–21. <https://doi.org/10.1016/j.jsg.2018.06.005>
- Ross, J., & Lewis, P. (1989). Brittle-ductile transition: Semibrittle behavior. *Tectonophysics*, 167, 75–79. [https://doi.org/10.1016/0040-1951\(89\)90295-3](https://doi.org/10.1016/0040-1951(89)90295-3)

- Ross, J. V., & Wilks, K. R. (1995). Effects of a third phase on the mechanical and microstructural evolution of a granulite. *Tectonophysics*, 241(3–4), 303–315. [https://doi.org/10.1016/0040-1951\(94\)00162-3](https://doi.org/10.1016/0040-1951(94)00162-3)
- Rostom, F., Royné, A., Dysthe, D. K., & Renard, F. (2013). Effect of fluid salinity on subcritical crack propagation in calcite. *Tectonophysics*, 583, 68–75. <https://doi.org/10.1016/j.tecto.2012.10.023>
- Rowe, K. J., & Rutter, E. H. (1990). Palaeostress estimation using calcite twinning: Experimental calibration and application to nature. *Journal of Structural Geology*, 12, 1–17. [https://doi.org/10.1016/0191-8141\(90\)90044-y](https://doi.org/10.1016/0191-8141(90)90044-y)
- Røyne, A., Bisschop, J., & Dysthe, D. K. (2011). Experimental investigation of surface energy and subcritical crack growth in calcite. *Journal of Geophysical Research*, 116(B4). <https://doi.org/10.1029/2010jb008033>
- Rummel, F. (1975). *Experimentelle Untersuchungen zum Bruchvorgang in Gesteinen*. Berchem Institute of Geophysics.
- Rutter, E. (1974). The influence of temperature, strain rate and interstitial water in the experimental deformation of Calcite rocks. *Tectonophysics*, 22, 311–334. [https://doi.org/10.1016/0040-1951\(74\)90089-4](https://doi.org/10.1016/0040-1951(74)90089-4)
- Rutter, E. H. (1986). On the nomenclature of mode of failure transitions in rocks. *Tectonophysics*, 122, 381–387. [https://doi.org/10.1016/0040-1951\(86\)90153-8](https://doi.org/10.1016/0040-1951(86)90153-8)
- Rutter, E. H. (1995). Experimental study of the influence of stress, temperature, and strain on the dynamic recrystallization of Carrara marble. *Journal of Geophysical Research-Solid Earth*, 100(B12), 24651–24663. <https://doi.org/10.1029/95jb02500>
- Rutter, E. H., & Schmid, S. M. (1975). Experimental study of unconfined flow of Solnhofen limestone at 500° to 600°C. *Geological Society of America Bulletin*, 86, 145–152. [https://doi.org/10.1130/0016-7606\(1975\)86<145:esoufo>2.0.co;2](https://doi.org/10.1130/0016-7606(1975)86<145:esoufo>2.0.co;2)
- Rybacki, E. (1986). *Der Übergang vom Spröbruch zum duktilen Fließen in Marmor*. (Diploma). Ruhr-University Bochum.
- Rybacki, E., Evans, B., Janssen, C., Wirth, R., & Dresen, G. (2013). Influence of stress, temperature, and strain on calcite twins constrained by deformation experiments. *Tectonophysics*, 601, 20–36. <https://doi.org/10.1016/j.tecto.2013.04.021>
- Rybacki, E., Herrmann, J., Wirth, R., & Dresen, G. (2017). Creep of posidonia shale at elevated pressure and temperature. *Rock Mechanics and Rock Engineering*, 50(12), 3121–3140. <https://doi.org/10.1007/s00603-017-1295-y>
- Rybacki, E., Janssen, C., Wirth, R., Chen, K., Wenk, H. R., Stromeyer, D., et al. (2011). Low-temperature deformation in calcite veins of SAFOD core samples (San Andreas Fault) -- Microstructural analysis and implications for fault rheology. *Tectonophysics*, 509(1–2), 107–119. <https://doi.org/10.1016/j.tecto.2011.05.014>
- Rybacki, E., Meier, T., & Dresen, G. (2016). What controls the mechanical properties of shale rocks? – Part II: Brittleness. *Journal of Petroleum Science and Engineering*, 144, 39–58. <https://doi.org/10.1016/j.petrol.2016.02.022>
- Rybacki, E., Morales, L. F. G., Naumann, M., & Dresen, G. (2014). Strain localization during high temperature creep of marble: The effect of inclusions. *Tectonophysics*, 634(0), 182–197. <https://doi.org/10.1016/j.tecto.2014.07.032>
- Rybacki, E., Reinicke, A., Meier, T., Makasi, M., & Dresen, G. (2015). What controls the mechanical properties of shale rocks? – Part I: Strength and Young's modulus. *Journal of Petroleum Science and Engineering*, 135, 702–722. <https://doi.org/10.1016/j.petrol.2015.10.028>
- Rybacki, E., Wirth, R., & Dresen, G. (2010). Superplasticity and ductile fracture of synthetic feldspar deformed to large strain. *Journal of Geophysical Research*, 115(B8), B08209. <https://doi.org/10.1029/2009jb007203>
- Schmid, S., Boland, J., & Paterson, M. (1977). Superplastic flow in finegrained limestone. *Tectonophysics*, 43, 257–291. [https://doi.org/10.1016/0040-1951\(77\)90120-2](https://doi.org/10.1016/0040-1951(77)90120-2)
- Schmid, S., Paterson, M., & Boland, J. (1980). High temperature flow and dynamic recrystallization in Carrara marble. *Tectonophysics*, 65, 245–280. [https://doi.org/10.1016/0040-1951\(80\)90077-3](https://doi.org/10.1016/0040-1951(80)90077-3)
- Schmocker, M., Bystricky, M., Kunze, K., Burlini, L., Stunitz, H., & Burg, J. P. (2003). Granular flow and Riedel band formation in water-rich quartz aggregates experimentally deformed in torsion. *Journal of Geophysical Research*, 108(B5), 2242. <https://doi.org/10.1029/2002JB001958>
- Scholz, C. (1968). Microfracturing and the inelastic deformation of rock in compression. *Journal of Geophysical Research*, 73, 1417–1432. <https://doi.org/10.1029/jb073i004p01417>
- Scholz, C. (1988). The brittle-plastic transition and the depth of seismic faulting. *Geological Society, London, Special Publications*, 77, 319–328. <https://doi.org/10.1007/bf01848693>
- Schubnel, A., Fortin, J., Burlini, L., & Gueguen, Y. (2005). Damage and recovery of calcite rocks deformed in the cataclastic regime. In D. Bruhn, & L. Burlini (Eds.), *High-strain zones: Structure and physical properties* (Vol. 254, pp. 203–221). The Geological Society of London. <https://doi.org/10.1144/gsl.sp.2005.245.01.10>
- Schubnel, A., Walker, E., Thompson, B. D., Fortin, J., Gueguen, Y., & Young, R. P. (2006). Transient creep, aseismic damage and slow failure in Carrara marble deformed across the brittle-ductile transition. *Geophysical Research Letters*, 33(17), L17301. <https://doi.org/10.1029/2006gl026619>
- Schuster, R., Habler, G., Schafner, E., & Abart, R. (2019). Microstructural and textural evolution of calcite deformed to high shear strain by high-pressure torsion. *Journal of Structural Geology*, 118, 32–47. <https://doi.org/10.1016/j.jsg.2018.09.003>
- Segurado, J., Lebensohn, R. A., & Llorca, J. (2018). Computational homogenization of polycrystals. In M. I. Hussein (Ed.), *Advances in crystals and elastic metamaterials, part 1* (Vol. 51, pp. 1–114). Elsevier. <https://doi.org/10.1016/bs.aams.2018.07.001>
- Shimada, M. (1993). Lithospheric strength inferred from fracture strength of rocks at high confining pressures and temperatures. *Tectonophysics*, 217, 55–64. [https://doi.org/10.1016/0040-1951\(93\)90202-u](https://doi.org/10.1016/0040-1951(93)90202-u)
- Shimamoto, T., & Noda, H. (2014). A friction to flow constitutive law and its application to a 2-D modeling of earthquakes. *Journal of Geophysical Research-Solid Earth*, 119(11), 8089–8106. <https://doi.org/10.1002/2014jb011170>
- Sibson, R. (1983). Continental fault structure and the shallow earthquake source. *Journal of the Geological Society London*, 140, 741–767. <https://doi.org/10.1144/gsjgs.140.5.0741>
- Siddiqi, G., Evans, B., Dresen, G., & Freund, D. (1997). Effect of semibrittle deformation on transport properties of calcite rocks. *Journal of Geophysical Research*, 102(B7), 14765–14778. <https://doi.org/10.1029/97jb01038>
- Spiers, C. J. (1981). Evidence for slip on  $r$  and  $f$  in the positive sense in deformed calcite single-crystals. *Journal of Structural Geology*, 3(2), 193.
- Stewart, M., Holdsworth, R. E., & Strachan, R. A. (2000). Deformation processes and weakening mechanisms within the frictional-viscous transition zone of major crustal-scale faults: Insights from the Great Glen Fault Zone, Scotland. *Journal of Structural Geology*, 22(5), 543–560. [https://doi.org/10.1016/S0191-8141\(99\)00164-9](https://doi.org/10.1016/S0191-8141(99)00164-9)
- Takagi, H., Goto, K., & Shigematsu, N. (2000). Ultramylonite bands derived from cataclastic and pseudotachylite in granites, northeast Japan. *Geological Society, London, Special Publications*, 22, 1325–1339. [https://doi.org/10.1016/s0191-8141\(00\)00034-1](https://doi.org/10.1016/s0191-8141(00)00034-1)
- ter Heege, J. H., de Bresser, J. H. P., & Spiers, C. J. (2002). The influence of dynamic recrystallization on the grain size distribution and rheological behaviour of Carrara marble deformed in axial compression. In S. de Meer, M. R. Drury, J. H. P. de Bresser, & G. M. Pennock (Eds.), *Deformation mechanisms, rheology and tectonics: Current status and future perspectives* (Vol. 200, pp. 331–353). Geological Society Special Publications. <https://doi.org/10.1144/gsl.sp.2001.200.01.19>

- Tommasi, A., Mainprice, D., Canova, G., & Chastel, Y. (2000). Viscoplastic self-consistent and equilibrium-based modeling of olivine lattice preferred orientations: Implications for the upper mantle seismic anisotropy. *Journal of Geophysical Research-Solid Earth*, *105*(B4), 7893–7908. <https://doi.org/10.1029/1999jb900411>
- Tullis, J., & Yund, R. (1992). Chapter 4 The Brittle-Ductile Transition in feldspar aggregates: An experimental study. In B. Evans, & T.-f. Wong (Eds.), *Fault mechanics and transport properties of rocks - a Festschrift in honor of W. F. Brace* (Vol. 51, pp. 89–117). Academic Press. [https://doi.org/10.1016/s0074-6142\(08\)62816-8](https://doi.org/10.1016/s0074-6142(08)62816-8)
- Valcke, S. L. A., de Bresser, J. H. P., Pennock, G. M., & Drury, M. R. (2015). Influence of deformation conditions on the development of heterogeneous recrystallization microstructures in experimentally deformed Carrara marble. *Geological Society, London, Special Publications*, *409*(1), 175–200. <https://doi.org/10.1144/sp409.4>
- Ván, P., & Vászárhelyi, B. (2010). Centenary of the first triaxial test – Recalculation of the results of Kármán. Paper presented at the ISRM International Symposium- EUROCK 2010 Lausanne, Switzerland.
- Verberne, B. A., Chen, J., Niemeijer, A. R., de Bresser, J. H. P., Pennock, G. M., Drury, M. R., et al. (2017). Microscale cavitation as a mechanism for nucleating earthquakes at the base of the seismogenic zone. *Nature Communications*, *8*(1), 1645. <https://doi.org/10.1038/s41467-017-01843-3>
- Verberne, B. A., Niemeijer, A. R., De Bresser, J. H. P., & Spiers, C. J. (2015). Mechanical behavior and microstructure of simulated calcite fault gouge sheared at 20–600 degrees C: Implications for natural faults in limestones. *Journal of Geophysical Research-Solid Earth*, *120*(12), 8169–8196. <https://doi.org/10.1002/2015jb012292>
- Verberne, B. A., van den Ende, M. P. A., Chen, J. Y., Niemeijer, A. R., & Spiers, C. J. (2020). The physics of fault friction: Insights from experiments on simulated gouges at low shearing velocities. *Journal of Geophysical Research-Solid Earth*, *11*(6), 2075–2095. <https://doi.org/10.5194/se-11-2075-2020>
- Violay, M., Gibert, B., Mainprice, D., Evans, B., Dautria, J. M., Azais, P., et al. (2012). An experimental study of the brittle-ductile transition of basalt at oceanic crust pressure and temperature conditions. *Journal of Geophysical Research-Solid Earth*, *117*(B3), B03213. <https://doi.org/10.1029/2011jb008884>
- Wallis, D., Hansen, L. N., Tasaka, M., Kumamoto, K. M., Parsons, A. J., Lloyd, G. E., et al. (2019). The impact of water on slip system activity in olivine and the formation of bimodal crystallographic preferred orientations. *Earth and Planetary Science Letters*, *508*, 51–61. <https://doi.org/10.1016/j.epsl.2018.12.007>
- Wang, H., Raeesinia, B., Wu, P. D., Agnew, S. R., & Tome, C. N. (2010). Evaluation of self-consistent polycrystal plasticity models for magnesium alloy AZ31B sheet. *International Journal of Solids and Structures*, *47*(21), 2905–2917. <https://doi.org/10.1016/j.ijssolstr.2010.06.016>
- Wendt, A. S., Mainprice, D., Rutter, E., & Wirth, R. (1998). A joint study of experimental deformation and experimentally induced microstructures of pretextured peridotites. *Journal of Geophysical Research*, *103*(B8), 18205–18221. <https://doi.org/10.1029/98jb01555>
- Wong, T. F., & Baud, P. (2012). The brittle-ductile transition in porous rock: A review. *Journal of Structural Geology*, *44*, 25–53. <https://doi.org/10.1016/j.jsg.2012.07.010>
- Xu, L. L., & Evans, B. (2010). Strain heterogeneity in deformed Carrara marble using a microscale strain mapping technique. *Journal of Geophysical Research*, *115*(B4), B04202. <https://doi.org/10.1029/2009jb006458>
- Yang, L., & Li, Z.-d. (2018). Nonlinear variation parameters creep model of rock and parametric inversion. *Geotechnical and Geological Engineering*, *36*(5), 2985–2993. <https://doi.org/10.1007/s10706-018-0517-8>
- Yu, H. H., Xin, Y. C., Wang, M. Y., & Liu, Q. (2018). Hall-Petch relationship in Mg alloys: A review. *Journal of Materials Science & Technology*, *34*(2), 248–256. <https://doi.org/10.1016/j.jmst.2017.07.022>
- Zoback, M. D. (2007). *Reservoir geomechanics*. Cambridge University Press.